Nanoscale

Accepted Manuscript

This article can be cited before page numbers have been issued, to do this please use: M. Pizzella, A. Accardo, F. A. Mercurio, T. Sibillano, E. Gallo, G. Morelli, G. Smaldone, C. Giannini, M. Leone, N. Balasco, C. Diaferia and L. Vitagliano, *Nanoscale*, 2025, DOI: 10.1039/D5NR02939B.

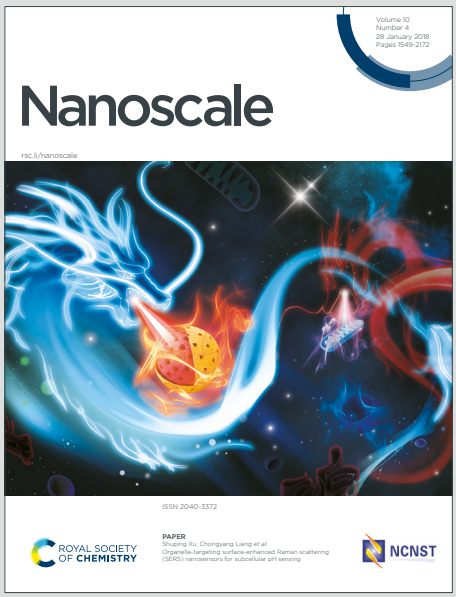

ROYAL SOCIETY OF CHEMISTRY

rsc.li/nanoscale

View Article Online
DOI: 10.1039/D5NR02939B

Structural and functional characterization of self-assembling fragments identified from the transthyretin amyloid-like structure

Mariantonietta Pizzella[1], Antonella Accardo[1], Flavia Anna Mercurio[2], Teresa Sibillano[3], Enrico Gallo[4], Giancarlo Morelli[1], Giovanni Smaldone[4], Cinzia Giannini[3], Marilisa Leone[2], Nicole Balasco[5*], Carlo Diaferia[1*], Luigi Vitagliano[2]

[1]Department of Pharmacy and Interuniversity Research Centre on Bioactive Peptides "Carlo Pedone" (CIRPeB), University of Naples "Federico II", Via T. De Amicis 95, Naples 80145, Italy.
[2]Institute of Biostructures and Bioimaging (IBB), CNR, Via P. Castellino 111, Naples 80131, Italy.
[3]Institute of Crystallography (IC), CNR, Via Amendola 122, Bari 70126, Italy.
[4]IRCCS SYNLAB SDN, Via G. Ferraris 144, Naples 80146, Italy.
[5]Institute of Molecular Biology and Pathology (IBPM), CNR, c/o Department Chemistry, Sapienza University of Rome, Piazzale Aldo Moro 5, Rome 00185, Italy.

[*]Correspondence should be addressed to C.D. (carlo.diaferia@unina.it) or N.B. (nicole.balasco@cnr.it).

Keywords: amyloid-like structures, nanostructures, self-assembling peptides, hydrogels

Abstract

The structural biology of amyloid-like systems has experienced significant advances due to the impressive technological and methodological advancements of experimental and computational techniques, providing unprecedented atomic-level details into the molecular architecture of these aggregates. Taking advantage of the availability of novel and complex amyloid-like protein structures, we evaluated the possibility of expanding the universe of self-assembling peptides by exploiting these structural data. We utilized transthyretin, a protein whose amyloid-like aggregation has significant pathological consequences but has never been employed to generate peptide-based materials, as a model system to develop a procedure for identifying novel self-assembling peptides. The pipeline we developed is based on the preliminary evaluation of the stability of the fragments through molecular dynamics simulations, experimental verification of the formation of cross-β assemblies in both solution and the solid state, and characterization of the functional properties of the generated biomaterial. In this framework, we demonstrate that selected transthyretin-based peptides have a strong tendency to self-assemble and form soft hydrogels. The characterization of these systems suggests that a mixture of these peptides tends to aggregate by co-assembly, mimicking the

View Article Online
DOI: 10.1039/D5NR02939B

interactions that stabilize the amyloid-like structure of the parent protein. Our data emphasize the role that local structures play in the mechanical and optical properties of these assemblies.

1. Introduction

Non-covalent interactions are fundamental forces that play a key role in the three-dimensional organization of biomolecules and in mediating their partnerships with other molecules and ions. One of the most striking manifestations of non-covalent interactions is the remarkable propensity of peptides and proteins to frequently undergo self-assembly, forming supramolecular assemblies with intricate architectures and uncommon thermal and chemical stabilities [1]. The most common basic structural element that characterizes these assemblies is the so-called cross-β motif, characterized by layers of β-sheet in which the polypeptide chains run perpendicularly to the growing axis of the fiber/aggregate [1,2]. Cross-β organizations were initially identified as the basic motif of the amyloid-like assembly commonly detected in severe and widespread neurodegenerative diseases [1,3]. The progressive biophysical and structural characterization of these systems has led to the discovery that polypeptide chains exhibit a remarkable propensity to form amyloid-like assemblies, even for very short peptides [4,5]. In this scenario, further characterizations of protein and peptide fragments have demonstrated that cross-β assemblies exhibit a repertoire of interesting mechanical, optoelectronic, and structural properties that make them attractive biomaterials for numerous applications [6–19]. The finding that similar structural entities play important roles in biomedicine and material science has led to a conspicuous osmosis of information between these distant areas [2]. Indeed, many findings and concepts developed in the structural biology of amyloids have been fruitfully employed to develop new biomaterials. On the other hand, the discovery that peptides, even dipeptides, and single amino acids, can form stable assemblies with varied physical manifestations, including fibers, hydrogels, and nanogels, has contributed to the understanding of the role of assemblies in biological contexts.

Initial atomic-level characterizations of amyloid-like systems were severely limited by the necessity to grow well-ordered crystals suitable for crystallographic investigations. This also limited the size of the systems that could be studied, as investigations were frequently restricted to peptides, which were merely models of the actual pathological protein agents. The technological and methodological innovations of the cryo-electron microscopy (cryo-EM) technique have rapidly changed this state. Indeed, in recent years, there has been an explosion of atomic-level structures of full-length proteins in their amyloid-like state [20–22].

In this scenario, we developed a procedure to identify new aggregation-prone protein fragments from structural data available in the Protein Data Bank (PDB) [20]. Specifically, we conducted a pilot study to demonstrate that fragments of the self-assembling protein transthyretin (TTR), whose amyloid-like

View Article Online
DOI: 10.1039/D5NR02939B

variants are associated with inherited transthyretin amyloidosis [23–25], a progressive and debilitating disease that can be ultimately fatal, could display interesting properties in their amyloid-like properties—even though this protein had never been previously considered for peptide-based biomaterial development. After extensive characterization of the dynamical properties of a TTR PDB amyloid structure, we selected specific fragments for further investigations. The extensive characterizations of TTR-based peptides confirmed their tendency for cross-β association and demonstrated their ability to form hydrogels with notable mechanical and spectroscopic properties.

2. Results

2.1 Searching the PDB for amyloid-like structures

To identify novel candidates for peptide-based materials endowed with a cross-β spine, we preliminarily surveyed the PDB for three-dimensional models of amyloid-like structures (supplementary **Table S1**). As detailed in the Methods section, the August 2024 database release was explored. As reported in **Figure 1A**, a significant increase in amyloid-like structures has been observed in the PDB over the last few years. The dissection of these structures according to the experimental technique used for their solution clearly indicates that this increase is essentially due to the impressive methodological advances of the electron cryo-microscopy (cryo-EM) technique. Indeed, while the number of structures determined by X-ray diffraction is roughly constant over the years, the number of cryo-EM structures is impressively increasing, approaching one hundred per year. Electron crystallography studies also provided a significant contribution to this increment. The classification of these structures as a function of the time of release and protein/peptide size highlights a remarkable increase in the size of the characterized systems (**Figure 1B**).

Among others, the amyloid-like structure that corresponds to the aggregation-prone variant of the protein TTR is particularly interesting. This protein, which forms a stable tetramer in its wild-type form (**Figure 2A** – PDB ID: 6SUG) [26], undergoes a dramatic structural transition when the residue Val50 is mutated to Met (**Figure 2B** – PDB ID: 7OB4) [27]. It is important to note that the structural conversion of the protein has major pathological effects. In the cryo-EM structure of the transthyretin fibril, a twisted dimer can be identified. Each unit of the dimer is characterized by two nearly independent assemblies (residues 31–55 and residues 77–143 of the UniProtKB P02766) that are stabilized by strong hydrophobic interactions. The tight association of its building components in the amyloid-like state and the fact that its tendency to form aggregates has never been previously exploited for generating biomaterials prompted us to use TTR fragmentation to identify novel self-assembling peptides.

DOI: 10.1039/D5NR02939B

2.2 Assessment of the stability of the selected TTR assemblies by Molecular Dynamics

To identify fragments of the TTR amyloid-like structure suitable for developing new peptide-based materials, we obtained some preliminary indications of their stability by conducting molecular dynamics (MD) simulations using, as a starting model, structures retrieved from the fibrillar cryo-EM model (see Methods for details). Two independent replicas (denoted as replica 1 and replica 2) were carried out for each investigated system. Although the timescales of each replica (200 ns – **Table S2**) are somewhat limited in providing thermodynamic estimates of the stability of these systems, we used this screening analysis as a guide for synthesizing and characterizing specific fragments.

Initial MD simulations were conducted on the entire dimeric fibrillar assembly (**Figure S1**). Despite the limited length of the simulations, we observed early major structural rearrangements of the starting model as indicated by the rapid increase in RMSD values (**Figure S2**). However, the inspection of the RMSD values computed on the two individual assemblies suggests that the major overall rearrangements correspond to a strong destabilization of the monomer-monomer interface in the dimer. The monitoring of the distance of representative atoms at the interface of the cryo-EM structure corroborates this observation. This distance, which is only 6 Å in the starting model, reaches values as high as 80 Å (**Figure S3**). In line with the low RMSD values calculated on the individual monomers, the β-structure of these assemblies is well preserved in the simulations (**Figure S4**).

Similar conclusions emerge from the simulation conducted on a single unit of the fibrillar assembly. Indeed, as shown in **Figures 3** and **S5**, trajectory structures present limited deviations compared to the starting model (RMSD ~ 2.5 Å). Moreover, the β-structure of the unit is well preserved throughout the simulation. The inspection of the RMSF (root mean square fluctuations) values suggests that the most rigid regions correspond to residues 44-49, 88-96, and 123-135 (**Figures 3C** and **S5B**). Since one of these regions is embedded in an isolated fragment of the structure (**Figure 2B**), we evaluated the stability of this specific fragment when extracted from the fibrillar assembly. This amyloid-like motif, in which single polypeptide chains form a β-hairpin structure, corresponds to the residues 34-52 and embodies the mutation Val50Met that favors the aggregation. The stability of this fragment, hereafter denoted as TTR^{34-52}, was also evaluated by MD. As shown in **Figure 4A**, this motif is stabilized by a hydrophobic interface involving a multitude of apolar residues, including Val34, Val36, Leu37, Val40, Ile46, Val48, Met50, and Val52. In parallel, to check the ability of this interface to keep residues of the two strands of the hairpin in close contact, we also considered in the MD simulations a variant of the parent fragment in which the turn (residues 41-44) that covalently links these extremities was removed. This novel model is formed by two interacting peptides, made of residues 34-40 (TTR^{34-40}) and 45-52 (TTR^{45-52}), and is globally denoted as TTR^{34-40}+TTR^{45-52} (**Figure 4B**). In both systems, the secondary structure (**Figures 4C-D** and **S6AB**) and the global shape of the

View Article Online
DOI: 10.1039/D5NR02939B

assembly (**Figure S7**) are well-preserved in the trajectory structures. Moreover, the RMSF values indicate that these assemblies are relatively rigid (**Figure S7**). Globally, these findings indicate that, in the timescale of the simulations, the structure of the assemblies is maintained, although, as expected, the TTR^{34-52} is endowed with a higher rigidity. Based on these results, the three peptides TTR^{34-52}, TTR^{34-40}, and TTR^{45-52} were selected for experimental studies.

2.3 Experimental characterization of the TTR-derived peptides

2.3.1 Peptide synthesis, solubility, and critical aggregation concentration

As detailed in the methods section, the TTR^{34-52} peptide was generated through solid-phase peptide synthesis on a Rink-amide resin, which allows the production of the peptide in its amidated form at the C-terminus. All the peptides were also acetylated at their N-terminus to simulate the conditions of peptide fragments in the parent protein. Similarly, we synthesized the two single peptides, TTR34-40 and TTR45-52, to investigate their structural and aggregative behavior, excluding the influence of the turn connecting the two strands of the hairpin (**Figure 5**). The peptides were then purified by RP-HPLC chromatography, and their identity was assessed by LC-MS (**Figures S8** and **S9**). Retention time and molecular weight experimentally determined for each peptide are reported in **Table S3**.

All peptides exhibited low solubility in water, with estimated solubilities of 1.0 mg/mL for TTR34-52 and TTR45-52, and 2.0 mg/mL for TTR^{34-40}. Fluorescence measurements were used to evaluate the propensity of peptides to self-assemble under these conditions. The critical aggregation concentration (CAC) value of the peptides dissolved in water was estimated using a well-assessed fluorescence method based on the titration of the fluorophore 8-anilinonaphthalene-1-sulfonate ammonium salt (ANS), with increasing amounts of peptides [28]. The characteristic of the ANS is its capability to emit fluorescence between 460 and 480 nm only in the presence of a hydrophobic environment, such as the inner micellar core or the aliphatic/aromatic interface of peptide nanostructures. The CAC value is easily extrapolated from the breakpoint of the graph in Figure 5, which reports the fluorescence of the ANS dye at 470 nm as a function of peptide concentration. All the CAC values are collected in **Table 1**. All the peptides exhibited CAC values of the same order of magnitude (10^{-4} mol/L). However, a trend related to solubility and peptide length is observed, with the lowest CAC value for the most extended sequence TTR^{34-52} ($1.11 \cdot 10^{-4}$ mol/L) and the highest CAC for the most soluble one (TTR^{34-40}, $5.42 \cdot 10^{-4}$ mol/L).

2.3.2 Hydrogel formulation

The capability of these peptides to self-assemble at concentrations above their water solubility was also evaluated by using the "solvent switch" method. This method requires the dissolution of the

View Article Online
DOI: 10.1039/D5NR02939B

peptide in an organic solvent such as HFIP or DMSO at 100 mg/mL and its subsequent dilution in water to achieve the desired concentration [13,29]. In our case, we used HFIP for the initial dissolution of each peptide sequence. The organic solvent was removed from the sample solution under N_2 flow, and this protocol was used to obtain samples for all the analyses (pH range 6.7-7.2 after preparation). By leaving the sample to age at room temperature, the formation of self-supporting hydrogels was observed for samples at 10 mg/mL (1.0 %wt). On the contrary, a viscous solution was observed at 5.0 mg/mL (0.5 wt%), whereas at lower concentrations, limpid solutions were obtained. Using the same method, we also prepared the mixed hydrogel of TTR^{34-40}+TTR^{45-52} at 1.0%wt (1/1, w/w ratio). The state of gel was initially deduced by the inverted test tube (**Figure 6A**), even associated with no syneresis phenomena, with a notably long shelf stability for all the samples, with no macroscopic or optical differences and no significant differences in optical transparency up to 6 months and confirmed by rheology tests (*vide infra*).

2.3.3 Structural characterizations in solution

The secondary structure of all the peptides was investigated by Circular Dichroism (CD) and Congo Red (CR) assays. These investigations are classically used to establish the presence of β-sheets (with parallel or antiparallel β-strands) in fibrillary peptide nanostructures. Initial CD characterizations of individual peptides TTR^{34-52}, TTR^{34-40}, and TTR^{45-52} and the TTR^{34-40}+TTR^{45-52} mixture were carried out at 1wt% (10 mg/mL, pH range 6.7-7.2) (**Figure 7**) (see methods for details). In these conditions, hydrogelation occurs for all samples. Far-CD spectra collected on these samples reveal the typical signature of β-sheet structure as indicated by a negative signal in the region of n-π* transitions. This band is centered at 223 nm for TTR^{34-40}, 226 nm for TTR^{34-52}, and red-shifted to 228 nm for TTR^{45-52}, thus indicating a stronger aggregative behavior for the latter. Moreover, the β-sheet organization is further confirmed by a positive signal at around 195–200 nm [30]. The minimum signal at 226 nm for TTR^{34-40}+TTR^{45-52} indicates that the two single strands, when mixed, could undergo an arrangement similar to that of the complete fragment TTR^{34-52}. The dichroic signal was also monitored at different temperatures in the range 30 ÷ 80 °C. The negative signal around 225 nm is preserved for all peptides, although it decreases slightly with increasing temperature. This finding indicates that these β-rich assemblies exhibit remarkable thermal stability, a feature that is somewhat expected for this type of structure.

The dilution of these samples resulted in a progressive gel-to-solution transition, accompanied by significant variations in the CD signals, as illustrated in **Figure S10** for the sample TTR^{34-40}. These changes are indicative of a progressive unfolding of the peptide. This observation prompted us to collect CD spectra in diluted conditions (1 mg/mL) for all samples (**Figure 8**). For all peptides, the

View Article Online
DOI: 10.1039/D5NR02939B

dilution led to a secondary structure transition with a shift of the minimum to ~ 200-203 nm. In all cases, in addition to this minimum, a shoulder at approximately 220 nm is observed. These features suggest that peptide systems are predominantly in an unfolded state with a minor content of helical structure (possibly a 3-10 helix). The increase in temperature for the samples in diluted conditions produces interesting effects. Indeed, in all cases, we observe a general variation in the relative intensity of the negative peaks at ~ 203 and 220 nm, favoring the latter. This indicates an increase in the structure as a function of temperature. The effect is particularly evident in the spectra collected on the peptide TTR^{34-40}, which, at high temperatures (~80 °C), assumes a regular α-helical structure with two minima at approximately 203 and 222 nm. The clear temperature-dependent structural transition is also demonstrated by the presence of an isodichroic point in these spectra, indicating a two-state (α-helix, random coil) population of this peptide [31]. Considering the intriguing behavior of this peptide, we also evaluated the effect of sample cooling on the CD signal. As shown in **Figure S11,** although the intensity of the spectrum is globally reduced, likely due to precipitation effects, the location of the minima upon cooling becomes similar to that detected at room temperature, indicating the (partial) reversibility of the process.

It is also worth mentioning that the spectra of the mixture TTR^{34-40}+TTR^{45-52} exhibit some specific features, such as the higher negative intensity of the peak at 220 compared to that observed at 203 nm, which is not present in either of the two component peptides. This mutual influence of the two peptides is likely indicative of intermolecular interactions.

The β-sheet organization in peptide solutions is also confirmed by the Congo Red (CR) assay. CR is an azoic dye commonly used for the identification of amyloid-like structures, both in solution and in the solid state [32]. In the presence of β-sheet structures, the characteristic absorption peak of CR is red-shifted from 485 to 530 nm. CR solution (0.8 mg/mL) was added to peptide solutions of single peptides (TTR^{34-40}, TTR^{45-52}, and TTR^{34-52}) or at the TTR^{34-40}+TTR^{45-52} mixture prepared at a concentration of 5.0 mg/mL, which represents the concentration at which all peptides are in their β-sheet structure. In line with expectations, the maximum in **Figure 9A** appears shifted compared with that observed for the CR alone. This effect is highlighted in the spectra, where the CR signal has been subtracted (**Figure 9B**).

2.3.4 Nuclear Magnetic Resonance studies

Next, we conducted conformational analyses of all peptides (TTR^{34-40}, TTR^{45-52}, TTR^{34-52}) and the TTR^{34-40}+TTR^{45-52} mixture by solution NMR (Nuclear Magnetic Resonance) spectroscopy. NMR studies were carried out for diluted and concentrated peptide samples at concentrations lower and ten times higher than the CAC, respectively. 1D [^{1}H] and 2D [^{1}H, ^{1}H] NMR spectra were recorded and

View Article Online
DOI: 10.1039/D5NR02939B

analyzed for all peptide samples. Almost complete proton resonance assignments were obtained at low concentrations (**Tables S4-S7**).

Interestingly, the NOESY [33] spectra of the TTR^{34-40} (**Figure S12**, right panel) and TTR^{45-52} (**Figure S13**, right panel) peptides appear canonical of disordered species. The NOE cross-peaks in the NOESY [33] spectrum of TTR^{34-40} present opposite signs compared to the diagonal ones, as is common for a small and flexible peptide (**Figure S12**, right panel). Reduced signal intensity dominates the NOESY [33] (**Figure S13**, right panel) and ROESY [34] (**Figure S13**, middle panel) spectra of TTR^{45-52}, possibly due to the reduced solubility of this peptide in comparison with TTR^{34-40}. Therefore, the 2D [^{1}H, ^{1}H] TOCSY [35] spectrum of the mixture TTR^{34-40}+TTR^{45-52} (**Figure S14**, left panel) appears almost identical to the sum of the separate spectra of the two isolated peptides demonstrating no evident interactions in between the two fragments as further confirmed by analysis of NOESY (**Figure S14**, right panel) [33] and ROESY (**Figure S14**, middle panel) [34] spectra. Regarding the TTR^{34-52} peptide (**Figures S15** and **S16**), the NOESY [33] spectrum contains more cross-peaks of the same sign as the diagonal peaks (**Figure S15** right panel), likely pointing to a more rigid conformation related to its bigger size and possibly to a minimal increase of ordered conformations.

To get further insights into residual secondary structure elements characterizing each peptide sample at the lowest concentrations chemical shift deviations of the observed Hα protons compared to the random coil ones were evaluated (**Figure S17A**) along with ROE patterns (**Figure S17B**). The ROE networks contain mainly sequential contacts of the $H\alpha_i$-HN_{i+1} type, indicative of random conformations (**Figures S16** and **S17B**)[36]. Despite the absence of NOE and ROE contacts clearly indicating the presence of specific secondary structure elements, chemical shift deviations from random coil values [37–39] appear mainly negative pointing out likely very small amounts of helical/turn conformations, however the fact that these deviations are small and mostly close to |0.1| ppm clearly demonstrates that the random/disordered state dominates within all these peptides (Figure S17A). Indeed, the percentages of helical populations within each peptide were evaluated based on CSD data of Hα protons [40] (See Material and Methods for further details) and resulted as follows: TTR^{34-40} 27.8%, TTR^{45-52} 24.7%, TTR^{34-52} 28%, TTR^{34-40}+TTR^{45-52} 27.4% + 24.7%.

Next, NMR spectra of peptides at increased concentrations were compared with those obtained under diluted conditions (**Figures S18** and **S19**). By raising concentration, no changes in the spectrum of the TTR^{34-40} peptide could be observed thus indicating that this is the peptide with the lowest tendency to aggregate (**Figure S18A**). Instead, chemical shift changes and/or line broadening occurred for the NMR samples containing the peptides TTR^{45-52} (**Figure S18B**), TTR^{34-52} (**Figure S18C**), and the mixture TTR^{34-40}+TTR^{45-52} (**Figures S18D and S19**). Gelation of the NMR samples of TTR^{45-52} and the mixture TTR^{34-40}+TTR^{45-52} was evident by raising the peptide concentrations as well.

View Article Online
DOI: 10.1039/D5NR02939B

A comparison of TOCSY spectra of the mixture TTR^{34-40}+TTR^{45-52}, recorded at 0.25 mg/mL and 3.1 mg/mL, demonstrated, by qualitative analysis, that, although gelation is inducing at the highest peptide concentration unspecific line broadening affecting all residue in both peptide fragments due to the increased sample viscosity, and consequent slower tumbling, the largest decrease in peak intensities correlates with the residues of the TTR^{45-52} fragment, and is particularly evident for A49 and M50, thus indicating that possibly the central region of the peptide might be more involved in driving the self-assembly (**Figure S19**).

Overall, these NMR data show that the fragment-driving aggregation corresponds to the TTR^{45-52} peptide. These results appear in perfect agreement with those obtained by CD and other experimental techniques.

Nevertheless, NMR studies of peptides at concentrations higher than the CAC do not allow us to gain information on the presence of cross-beta amyloid-like fibers. This is not surprising, as larger molecular weight aggregates and prefibrillar species are fast-relaxing and thus not visible by solution NMR techniques. Consequently, what is observed by NMR analyses of the TTR peptides at the highest concentrations is likely to consist of more soluble monomers and smaller aggregates that appear mainly disordered, like the same peptides under diluted conditions in the isolated forms [41,42].

2.4 Structure prediction and dynamics of TTR-derived peptides

2.4.1 AlphaFold predictions of the single chain and multiple chain assemblies

To gain insights into structure-property relationships, we generated structural models of TTR^{34-52}, TTR^{34-40}, TTR^{45-52}, and their combination, TTR^{34-40}+TTR^{45-52}, using AlphaFold3 (AF) [43]. For each system, two separate predictions were made: one for single-chain models, which may represent the diluted conditions, and the other for multi-chain assemblies (16 strands), which could accurately depict the aggregated states.

As shown in **Figure 10**, helical conformations were predicted with high confidence, as estimated by a value of the per-residue Local Distance Difference Test (pLDDT) [44] larger than 70, for the individual peptides TTR^{34-52} and TTR^{45-52}. In contrast, TTR^{34-40} does not adopt a regular secondary structure in the AF model. Notably, the mixing of TTR^{34-40} and TTR^{45-52} results in the prediction of a β-sheet with very high confidence (pLDDT > 90). When multi-chain assemblies were considered, models featuring β-sheet structures were predicted (**Figure 10**). For the $TTR^{34–52}$ peptide, the AF model closely matches the structure of this fragment in the experimental structure of the TTR protein (PDB ID: 7OB4). Additionally, when multiple chains of $TTR^{45–52}$ were considered, a high-confidence model featuring a parallel orientation of the strands in the two facing sheets was observed. In contrast, less regular β-sheet structures were predicted for $TTR^{34–40}$ alone and its mixture with $TTR^{45–52}$,

View Article Online
DOI: 10.1039/D5NR02939B

although these predictions were associated with low-confidence pLDDT values. From these predictions, it emerges that $TTR^{34–40}$ shows a preference for the antiparallel association of strands within the sheet, whereas $TTR^{45–52}$ favors a parallel orientation. This is also evident in the $TTR^{34–40}$+$TTR^{45–52}$ model, in which the two peptides assemble into alternating layers, forming a mixed β-sheet structure with distinct strand orientations that reflect the preferences of each peptide.

To gain insights into the reliability of the AF models, we compared the experimental CD described in the previous paragraphs with those computed using the predicted structures as models (**Figure S20**). Although some of the single-chain models are characterized by rather good values of the auto-evaluation pLDDT score of AF, the corresponding simulated CD spectra are somewhat different from the experimental one. This suggests that AF models are not good representative models of the structure that these peptides assume in diluted conditions. Moreover, these data are in agreement with NMR results, indicating that the helical content in the isolated peptides at concentrations below the CAC is very low, and they are instead mainly disordered in solution. A better agreement between the experimental and the computed CD spectra is observed for the multichain assemblies. Indeed, in both cases, a single negative peak is detected. However, the wavelength of these minima is not coincident (**Figure S20**). Among other factors, this difference may be due to the different sizes of the assemblies which are likely underestimated in the computed models compared to the experimental ones.

2.4.2 Dynamics of the AlphaFold models

Considering the limited success of the AF predictions in interpreting the structural versatility of these peptides, we extended these analyses by performing MD simulations on both single and multi-chain systems using the AF structures as starting models. The study of the secondary structures of the single-chain AF models reveals that they possess remarkable flexibility, characterized by a limited content of regular structures. Indeed, the regular structure motif of the starting AF model is rapidly lost during the simulations in both replicas **(Figures 11A-D** and **S21A-D)**. On the other hand, the MD simulations carried out on the multichain assemblies show that, in the timescale of the simulation, their β-structure is well preserved **(Figures 11E-G** and **S21E-G)**. The least stable aggregate is the one formed by $TTR^{34–40}$, whose reliability, as expressed by the pLDDT values of AF, was limited.

The trajectory structures that emerged from these simulations were used to generate computed CD spectra. As shown in **Figure S20**, the agreement between these MD-based computed spectra and the experimental ones is very good for the single-chain systems. This indicated that the MD simulations provide a good representation of the intrinsic structural properties of the peptides in diluted conditions and corroborate the importance of combining predictive and dynamic data. For multi-chain

View Article Online
DOI: 10.1039/D5NR02939B

assemblies, since the AF structural motifs are well-preserved in the simulation, the MD structures yield similar CD spectra.

2.5 Characterization of the hydrogel and the xerogel

As reported in the previous paragraph, upon increasing the concentration of these peptides above their water solubility, the formation of hydrogels was observed. To gain insights into their mechanical and structural properties, we performed extensive characterization using a combination of different experimental techniques. Rheology experiments were carried out directly on the hydrogels in their native state. The other characterizations were conducted on xerogels, which were obtained by drop casting the hydrogel samples that had been dried overnight at room temperature.

2.5.1 Hydrogel characterization by rheology

These experiments were conducted to determine the viscoelasticity parameters, specifically G' (elastic or storage modulus) and G'' (viscous or loss modulus), for all systems. Dynamic strain sweeps in a 0.01-100% strain range (at ν= 1.0 Hz; **Figures 6B-E**) showed a linear viscoelastic region (LVR) in matrices, indicating stable gel formation due to the G'> G'' moduli relation [45]. TTR^{34-40}, TTR^{45-52}, and TTR^{34-40} + TTR^{45-52} hydrogels are characterized by shorter LVR, approximately in the 0.01-0.2% range, compared to TTR34-52 (0.01-2.0%). Even if TTR^{34-52} is the only hydrogel characterized by a critical value of oscillation (ω = 6.5%) in the tested range, it resulted as having a better elastic behavior with the highest G' value (G'=1172 Pa; G''= 130 Pa) if compared to TTR^{34-40} (G'=51 Pa; G''= 9 Pa), TTR^{45-52} (G'=13 Pa; G''= 3.5 Pa), and TTR^{34-40} + TTR^{45-52} (G'=70 Pa; G''= 15 Pa). As reported for other peptide-based and physically cross-linked hydrogels, all the transthyretin-based matrices have a soft nature, as suggested by the tan δ (G''/G') values (0.110, 0.176, 0.291, and 0.212 for TTR^{34-52}, TTR^{34-40}, TTR^{45-52}, and TTR^{34-40}+TTR^{45-52}, respectively). As expected, the mutual analysis of G' values indicates that TTR^{34-52}, representing the full-length hairpin primary sequences, has the best mechanical response if compared to the shorter ones. Interestingly, a cooperative effect can be envisioned in the viscoelastic features of the mixed TTR^{34-40}+TTR^{45-52} hydrogel. Moreover, the higher value of G' as the mean value of tanδ in comparison to TTR^{34-40} and TTR^{45-52} could suggest a co-assembly supramolecular pathway in this sample.

2.5.2 Xerogel characterization

2.5.2.1 Spectroscopic properties

FT-IR spectroscopy was used to support the indications derived from CD experiments and gain further insights into the structural features of these biomaterials. The measurements were conducted

View Article Online
DOI: 10.1039/D5NR02939B

on xerogels to reduce the water contribution of asymmetric and symmetric O–H stretching, thus increasing both the amide A (3277 cm^{-1}) and B N–H bands stretching resolution (2960 cm^{-1} for TTR^{34-40}, 2967 cm^{-1} for TTR^{45-52}, 2965 cm^{-1} for TTR^{34-52} and TTR^{34-40}+ TTR^{45-52}) (**Figures S22-S23**). The band located at ~1545 cm^{-1} in amide II is a consequence of the vibrations on the plane of the N–H bond and C-N stretching. Additional C-N stretching vibrations and N–H deformation are responsible for the bands centered at 1440 cm^{-1}. Additionally, for all the peptides, two peaks can be identified in the Amide I spectral region (1600-1700 cm^{-1}), associated with carbonyl stretching modes and reported to be the most intense and helpful in analyzing the secondary structure. The prevalence of β-sheet structuration is reinforced by the presence of similar bands (~1643 and ~1670 cm^{-1}) in absorbance deconvolution profiles (**Figure S23**) [46].

As previously described, the CR assay was also performed at the solid state, as it generates dichroic and birefringent effects under cross-polarized light sources with various colorations of the samples due to the staining *via* both hydrophobic and electrostatic interactions. The samples were placed on slides and, after a drying process, stained with a saturated CR solution and observed under a microscope using cross-polarized light (**Figure S24**). From the inspection of the figure, we can assess the positivity of the assay for all samples, with more evident apple-green birefringence for TTR^{45-52}.

2.5.2.2 Structural characterization by SEM and WAXS

The supramolecular structure of the assemblies was further examined through scanning electron microscopy (SEM) and wide-angle X-ray scattering (WAXS).

SEM characterization, performed on xerogels drop-casted onto aluminum stubs, confirmed a supramolecular organization typical of peptide-based hydrogels with interconnected fibrillary networks (**Figures 12** and **S25**).

WAXS measurements were performed on macroscopic fibers obtained using the stretch-frame method. Consistent with other experimental characterizations and modeling data, all WAXS patterns exhibit the hallmark features of the cross-β structural motif (**Figure 13** and **Table 2**). Specifically, a sharp meridional peak at 4.7 Å, which corresponds to the inter-strand distance in the β-sheet motif, invariably accompanied by an equatorial peak at 9-11 Å (**Table 2**), indicative of the inter-sheet distance between facing β-sheets. Notably, these distances closely align with the models derived from our computational studies. A third characteristic feature of the cross-β motif is a peak at ~ 3.2-3.7 Å, which likely corresponds to the length of the backbone per residue in the extended β-conformation.

Within this framework, the peptide TTR^{34-40} displays unique structural specificities. Indeed, in this system, a distinct equatorial peak appears at 5.2 Å. Given that this peptide can adopt an α-helical structure under specific conditions, this diffraction signal may correspond to the helical pitch oriented

View Article Online
DOI: 10.1039/D5NR02939B

perpendicularly to the fiber axis. This structural versatility suggests the presence of multiple conformational states within the fibers. Such heterogeneity is further supported by the complex, multi-peaked diffraction pattern observed in the 9-15 Å region, whereas other peptides typically exhibit a single diffraction peak (**Figure 13**).

2.5.2.3 Intrinsic fluorescence

Since several studies carried out over the last two decades have shown that cross-β structural motifs are endowed with a non-canonical intrinsic fluorescence whose emission falls in the visible regions [7,10,47] we explored the photoemissive behavior of peptide xerogels. As shown in **Figure 14**, a visible fluorescence was detected upon UV-visible excitation despite the absence of aromatic residues in the peptide sequences. Indeed, all systems present a rather strong green fluorescence. On the other hand, the blue fluorescence is strong in the peptides TTR^{34-40} and TTR^{45-52} while only the peptide TTR^{45-52} displays a remarkable red fluorescence. Surprisingly, the two systems TTR^{34-52} and TTR^{34-40}+TTR^{45-52}, which contain the highly fluorescent TTR^{34-40} and TTR^{45-52} fragments, present reduced emission in the blue and red regions. These findings highlight the importance of the supramolecular structure, which may depend on the specific context, in determining the fluorescence emission properties.

3. Discussion

In the last decade, structural biology has experienced two major revolutions. The impressive technological and methodological advancements of the Cryo-EM have impressively expanded the applicability of this technique and allowed the characterization of molecularly huge systems and/or fibrous assemblies generally precluded to X-ray crystallography [21,22]. More recently, this has been followed by the development of machine learning-based approaches that have greatly improved the reliability of computationally generated *ab initio* protein/peptide models.

Within the framework of the osmosis of information between structural biology and biomaterial science, we selected fragments from the PDB amyloid-like structure of the protein TTR, which is responsible for inherited transthyretin amyloidosis [23,24], that, according to our MD simulations, had the potential for self-assembling in cross-β structures. With the dual goal of creating a pipeline to find new aggregation-prone systems and produce new biomaterials, we experimentally validated these suggestions. Extensive characterization in solution and at the solid state of these peptides fully confirmed this prediction. Indeed, colorimetric assays using Congo Red and CD spectra confirmed the amyloid-like nature of the assemblies of the TTR-derived peptides. In particular, the CD spectra showed a fully reversible structural and physical-state transition as a function of concentration. Indeed, while these fragments are soluble and highly flexible at low concentrations, they undergo a

View Article Online
DOI: 10.1039/D5NR02939B

solution-gel transition coupled with the formation of β-structure upon concentration increase. For one of these peptides (TTR^{34-40}), an unusual conversion from the disordered to the α-helical state is observed upon temperature increase. Therefore, the highly versatile TTR^{34-40}, whose structure changes as a function of different environmental parameters, may constitute an interesting system for studying the determinants of structural conversions of peptides. Building on the innovative AlphaFold3 predictions [43], we attempted to gain atomic-level information on the different states of the peptides. Using the CD data as a validation tool, we found that AF overestimates the ordered structure of individual fragments, while it provides a satisfactory representation of the amyloid-like assemblies. The intrinsic, aggregation-free, structural propensities of these peptides are better captured by performing MD simulations starting from the AF models. Predicted and MD models of the assemblies are in good agreement with the WAXS data collected on xerogels. Indeed, not only are the inter-strand distances (~ 4.7 Å) in close agreement, but also the inter-sheet ones (~ 9-11 Å) are well replicated in computational studies.

The characterization of the hydrogel and the derived xerogels provides interesting clues on the mechanical and spectroscopic properties of these biomaterials [48]. Rheology experiments indicate the soft nature of the hydrogels and that the longest peptide (TTR^{34-52}) presents the best mechanical properties. Moreover, a comparative analysis of the G' values of TTR^{34-40}+TTR^{45-52} and the sum of single shorter peptide fragments (TTR^{34-40} and TTR^{45-52}) indicates that in the former a co-assembly [49] of the two composing peptides occurs. This is in line with the design procedure we employed, as these fragments are highly interconnected in the parent structure of the full-length TTR amyloid form. Finally, a comparative analysis of the variegated intrinsic fluorescence emission of these aggregates highlights the role of the local structure and interactions in their spectroscopic properties. Indeed, the two single peptides (TTR^{34-40} and TTR^{45-52}) present a wide emission that is partially lost when they are coupled either covalently (TTR^{34-52}) or non-covalently (TTR^{34-40}+TTR^{45-52}).

Collectively, we provide proof of concept that fragments extracted from amyloid structures present in the PDB can be successfully exploited to generate new biomaterials based on self-assembling peptides. The pipeline we delineate here is based on the following steps: (i) a preliminary evaluation, via MD simulations, of the stability of the fragments identified in the PDB (in silico steps); and (ii) an experimental assessment of the formation of cross-β assemblies, both in solution and in the solid state, along with the characterization of the functional properties of the resulting biomaterial (in vitro steps) (**Figure S26**).

In conclusion, peptide-based supramolecular entities represent intricate architectures that are rapidly gaining attention. Indeed, they offer interesting properties such as biocompatibility, biodegradability, modularity, and tunability. Potential applications of peptide-based biomaterials are related to the

View Article Online
DOI: 10.1039/D5NR02939B

development of extracellular matrix mimicking scaffolds for tissue engineering, of porous systems for drug delivery, films for optoelectronics, and water purification, as well as wound healing materials with antimicrobial profiles. However, the discovery of effective peptide-based materials is a lengthy process that requires multidisciplinary investigations. In this framework, leveraging the self-assembling potential of structurally characterized protein fragments could provide a reservoir of systems whose characterization and tuning may eventually lead to new, attractive biomaterials.

4. Methods

4.1 Chemicals

Rink amide MBHA (4-methylbenzhydrylamine) resin, coupling reagents and protected N^{α}-Fmoc-amino acid derivatives are commercially available from Calbiochem-Novabiochem (Laufelfingen, Switzerland). All other chemical products were purchased from Merck (Milan, Italy), Iris Biotech GmbH (Marktredwitz, Germany) or Labscan (Stillorgan, Dublin, Ireland) and they were used as delivered, unless stated otherwise.

4.2 PDB search of amyloid-like structures

The search for amyloid-like assemblies present in the Protein Data Bank (PDB) was performed by interrogating the entire database using the following criteria: Polymer Entity Type = "Protein"; Experimental Method = X-ray diffraction, electron microscopy, electron crystallography, solid-state NMR, fiber diffraction, neutron diffraction, solution scattering; Additional Structure Keywords = "amyloid"; Polymer Entity Sequence Length > 5. The PDB structures identified by the server were then manually inspected to verify that they correspond to amyloid-like cross-beta assemblies. The search of the PDB (August 2024 release) identified as many as 592 amyloid-like structures (**Table S1**).

4.3 Systems and predictions

The aggregation-prone variant of the protein transthyretin (TTR, UniProtKB P02766) carrying the Val50Met mutation was analyzed in the present study. The cryo-EM PDB structure of TTR amyloid fibrils (PDB ID: 7OB4) was used to generate the fibrillar models. Specifically, the study considered the double and single assemblies, as well as the extracted protein fragments: the β-hairpin formed by residues 34–52 ($TTR^{34–52}$) and the interacting sheets containing residues 34–40 and 45–52 ($TTR^{34–40}$+$TTR^{45–52}$). Structural models of TTR^{34-52}, TTR^{34-40}, TTR^{45-52}, and the combination TTR^{34-40}+TTR^{45-52} in both the single-chain and multi-chain states were predicted using the AlphaFold3 algorithm (https://alphafoldserver.com/) with default settings [43]. The best predicted model (model 0)

View Article Online
DOI: 10.1039/D5NR02939B

out of the five computed by AF was considered. The reliability of the AF predictions was assessed by analyzing the per-residue Local Distance Difference Test (pLDDT) [44] and the Predicted Aligned Error (PAE) matrices reported for each predicted structure.

4.4 Molecular dynamics

The GROMACS software was used to perform MD simulations on the structural models [50]. Amber99sb and TIP3P were used as force field and water model, respectively. The systems were solvated with water molecules in triclinic boxes. Counterions were added to balance charges. MD parameters of the simulations (box dimensions, number of water molecules and ions) are reported in **Table S2**. Electrostatic interactions were computed using the particle-mesh Ewald (PME) method with a grid spacing of 1.2 Å and a relative tolerance of 10^{-6} [51]. A 10 Å cut-off was applied for the Lennard-Jones (LJ) interactions. The LINCS algorithm was used for constraining bond lengths. The systems were initially energy minimized using steepest descent (50,000 steps) and then equilibrated in two phases. In the first step, systems were heated to 300 K temperature for 500 ps (NVT). Then, the pressure was equilibrated at the value of 1 atm for 500 ps (NpT). The Velocity Rescaling and Parrinello-Rahman algorithms were used to control temperature and pressure, respectively. The MD production runs were carried out at constant temperature (300 K) and pressure (1 atm) with a time step of 2 fs. The analysis of trajectory structures was performed by using GROMACS tools and the VMD program [52].

4.5 Peptide synthesis

The three peptide sequences (TTR^{34-40}, TTR^{45-52}, and TTR^{34-52}) were obtained through standard SPPS (solid-phase peptide synthesis) methodology using the Fmoc/tBu strategy. The Rink-amide MBHA resin, with a substitution rate of 0.70 mmol/g, was used as solid-phase support. Each peptide sequence was synthesized in *N,N*-dimethylformamide (DMF) using a scale of 0.25 mmol. The resin was left to swell in DMF for 30 min, the Fmoc protecting group was removed by treatment with 30% (v/v) piperidine and 1% DBU (v/v) in a DMF/NMP (1-metil-2-pirrolidone) for five cycles of 3 min each. A 2-fold molar excess of the Fmoc-protected amino acid was used for each coupling and solved in DMF together with equimolar amounts of 1-[Bis(dimethylamino)methylene]-1*H*-1,2,3-triazolo[4,5-*b*]pyridinium 3-oxid hexafluorophosphate, *N*-[(Dimethylamino)-1*H*-1,2,3-triazolo-[4,5-*b*]pyridin-1-ylmethylene]-*N*-methylmethanaminium hexafluorophosphate *N*-oxide (HATU), and a 4-fold molar excess of diisopropylethylamine (DIPEA). Each coupling was performed twice for 25 min under stirring at room temperature. The N-terminus of each sequence was acetylated with a solution of pyridine/acetic anhydride (4/4.7 v/v) in DMF (each treatment for 10 min) in two cycles of treatment.

View Article Online
DOI: 10.1039/D5NR02939B

At the end of the procedure, the resin was dried in diethyl ether and the crude peptides were fully cleaved by treating the peptidyl resin with a TFA (trifluoroacetic acid)/TIS (triisopropylsilane)/H_2O (92.5/5/2.5 *v/v/v*) mixture for 3h at room temperature. Cold ether was used to precipitate the peptides, which were freeze-dried three times. Pure peptides were obtained *via* RP-HPLC chromatography with a Agilent 1260 Infinity II Manual Preparative LC System (Agilent, Santa Clara, CA, USA) equipped with UV lambda-Max Model 481detector, using a Phenomenex (Torrance, CA, USA) C18 column. The flow rate was set at 20 mL/min and the elution solvents were H_2O/0.1% TFA (A) and CH_3CN/0.1% TFA (B) with (B) increasing from 20 to 80 % over 30 min. Analytical RP-HPLC analysis was used to assess the purity of peptides. Peptides were eluted from a C18 column using (A) and (B) as solvents and a method providing the increase of (B) percentage from 20 to 80% over 20 min at a flow rate of 1 mL/min. The identity of peptides was confirmed by MS spectrometry performed by using a LTQ XL Linear Ion Trap Mass Spectrometer, source ESI.

4.6 Sample preparation

The peptide solutions were prepared by simply dissolving powders in water or by the solvent-switch method. In detail, stock solutions of each peptide were prepared by dissolving the powder in 1,1,1,3,3,3-hexafluoro-2-propanol (HFIP) at a nominal concentration of 100 mg/mL. Subsequently, this solution was added to water at the desired concentration (between 1.0 and 10 mg/mL) and then, the HFIP was removed from the solution by a N_2 flow. Samples present a pH in the range 6.7-7.2 after preparation.

4.7 Fluorescence measurements

By titrating the dye 8-anilino-1-naphthalene sulfonic acid ammonium salt (ANS) with increasing concentrations of the peptide solution, the critical aggregation concentration (CAC) values for each peptide sequence were determined. After excitation of the samples at 350 nm, the fluorescence spectra were collected between 360 and 600 nm using a Shimadzu RF 6000 spectrofluorometer (Shimadzu, Kyoto, Japan). Small aliquots of peptide derivatives were added to 150 µL of a 20 µmol\L ANS water solution. Fluorescence spectra were corrected for the blank and adjusted for the dilution. CACs values were extrapolated at the breaking point of curves obtained by plotting the fluorescence emission at 470 nm as function of peptide concentration.

Aggregation kinetics of peptides, prepared as above reported, were followed by using a FLUOstar® Omega (BMG LABTECH) microplate reader. 100 µL of each sample were placed in wells of a 96-well plate and covered with an aluminum foil to avoid evaporation of the solvent. Experimental settings were: λ_{ex}=355 nm, gain 1000, bottom optic, orbital shake 200 rpm between readings.

View Article Online
DOI: 10.1039/D5NR02939B

Emission intensity at 460 nm was recorded over 300 hours and subtracted for the blank. Experiments were conducted in triplicates.

4.8 Rheological studies

Rheological properties of samples were evaluated using a rotational controlled stress rheometer (Malvern Kinexus) using a 15 mm flat-plate geometry (PU20:PL61). Freshly prepared samples (500 µL) at a concentration of 1.0 wt% and 0.1% wt were tested. Each experiment was performed at 25 °C using a humidity chamber and a gap of 1 mm. Preliminary dynamic rheological tests were carried out in order to identify the regime of linear viscoelasticity. The viscous elastic region was determined by the oscillatory frequency (0.1–100 Hz) and the strain sweep (0.01–100%). A time-sweep oscillatory evaluation test (using a constant 0.1% strain and 1 Hz frequency) was then performed for 20 min. Results are reported in Pascal (Pa) as shear Storage or elastic modulus (G') and shear loss or viscous modulus (G").

4.9 Circular Dichroism (CD) spectroscopy

Peptide samples at 10 mg/mL and 1 mg/mL concentrations, which were prepared as reported in paragraph 4.6, were placed in a 0.2 quartz cell (Hellma). Far-UV CD spectra were collected through a Jasco J-1500 spectropolarimeter equipped with a CTU100 thermal controller unit at 25°C. Spectra were recorded from 280 to 190 nm. 0.5 nm step, 2 nm bandwidth, 2 s collection time per step. Each spectrum was obtained by averaging three scans and corrected for the blank. The spectra in optical density were converted into molar ellipticity (Θ, expressed as deg cm^2 $decimol^{-1}$) by using the following formula: [Θ] = millidegrees/ (pathlength in millimeters × concentration in mol L^{-1} × number of peptide bonds). The number of peptide bonds are 18, 6, 7 and 13 for TTR^{34-40}, TTR^{45-52}, TTR^{34-52} and TTR^{34-40}/TTR^{45-52}. Temperature\wavelength scan was acquired at 1.0 mg\mL and 10 mg\mL at 30° C, 40° C, 50° C, 60° C, 70° C and 80° C.

CD spectra were calculated by using the Structure-Based Empirical Spectrum Calculation Algorithm (SESCA, https://www. mpinat.mpg.de/sesca) developed by Grubmüller et al. [53]. The default DS-dT basis set library containing three basis spectra (named Alpha, Beta, and Coil) were used. The CD spectra were calculated, providing either the AF predicted models or the MD trajectories (in PDB format) as the input.

4.10 Fourier Transform Infrared (FTIR) spectroscopy

FTIR spectra for dried samples were collected using a Jasco FT/IR 4100 spectrometer (Easton MD) in duplicate by using two different samples. Peptide samples at 10 mg/mL were fixed into a Specac

View Article Online
DOI: 10.1039/D5NR02939B

Pearl liquid cell with CaF_2 plates. For the acquisitions, liquid solutions were left to dry overnight at room temperature on the cells before the experiment was carried out. Each sample was subjected to a total of 128 scans. Spectra were collected over the range of 900 – 4000 cm^{-1}. Quantitative multivariate analysis for secondary structure estimation was conducted by a Jasco SSE software applying a method of principal component regression (PCR).

4.11 Congo Red (CR) spectroscopic assay

Congo Red spectroscopic assay was performed using UV/Vis Thermo Fisher Scientific Inc. (Wilmington, USA) nanodrop 2000c spectrophotometer equipped with 1.0 cm quartz cuvette; 10 µL of a water solution of CR (0.8 mg/mL) were freshly prepared and added to 800 µL of 5 mg/mL peptide solution. After 30 s of vortex and incubation of 5 min, spectra were recorded between 400 and 700 nm at room temperature. The CR spectrum at the same final concentration was used as reference and algebraically subtracted.

4.12 Birefringence CR polarized optical assay

On a microscope slide, 30 µL of each peptide sample (10 mg/mL) were placed, allowed to air-dry, and then stained with a saturated CR aqueous solution. After an overnight drying, the samples were observed with an OptechMB80-Pol microscope under bright-field illumination and between crossed polars.

4.13 Wide-Angle and Small-Angle X-Ray Scattering (WAXS)

WAXS patterns were obtained from solid fibers created using the stretch frame method [54]. About 20 µL of freshly prepared metastable peptide solutions (with a final gel concentration of 1.0 wt%) were placed between the ends of a wax-coated capillary, spaced 1.5 mm apart. The droplet was allowed to air-dry overnight, resulting in solid fibers [55]. Two-dimensional WAXS data were collected from these fibers at the X-ray MicroImaging Laboratory (XMI-L@b), using a Fr-E + SuperBright rotating anode tabletop microsource (Cu Kα, λ = 0.15405 nm, 2475 W), equipped with multilayer focusing optics (Confocal Max-Flux, CMF 15-105) and coupled to a three-pinhole camera (Rigaku SMAX-3000) [56,57]. WAXS data were acquired using an Image Plate (IP) detector (250 × 160 mm^2, 100 µm effective pixel size) placed at a ~10 cm distance from the sample to collect data in a range of 1.8–21 Å in direct space (0.3–3.5 $Å^{-1}$ in reciprocal space).

4.14 Scanning Electron Microscopy (SEM)

View Article Online
DOI: 10.1039/D5NR02939B

Morphological analysis of xerogels was carried out using field emission scanning electron microscope (Phenom Pro X G6, Netherlands, 450-FEI). Gels were placed on an aluminum stub using a graphite adhesive tape. A gold thin coat (7 nm) was sputtered at a current of 20 mA for 60 s. Images were acquired at an accelerating voltage of 15 kV, 1.0 Pa vacuum, through a SED Detector.

4.15 Nuclear Magnetic Resonance (NMR) spectroscopy

NMR experiments were acquired on a Bruker AVANCE NEO 500 MHz spectrometer equipped with a PRODIGY cryoprobe at a temperature of 25 °C. NMR samples consisted of peptides dissolved in H_2O/D_2O (deuterium oxide, 98% D, Sigma-Aldrich, Milan-Italy) 90/10 v/v at the following concentrations: TTR^{34-40} 0.2 mg/mL and 4.2 mg/mL, TTR^{45-52} 0.3 mg/mL and 2.1 mg/mL, TTR^{34-52} 0.6 mg/mL and 2.2 mg/mL, and TTR^{34-40}+TTR^{45-52} 0.25 mg/mL and 3.1 mg/mL. In details for each sample the following spectra were recorded:1D [^{1}H], 2D [^{1}H, ^{1}H] TOCSY [35] (Total Correlation Spectroscopy), 2D [^{1}H, ^{1}H] NOESY [33] (Nuclear Overhauser Enhancement Spectroscopy), 2D [^{1}H, ^{1}H] ROESY [34] (Rotating-Frame Overhauser Enhancement Spectroscopy), 2D [^{1}H, ^{1}H] DQFCOSY [58] (Double Quantum-Filtered Correlation Spectroscopy). TOCSY spectra were acquired with 70 ms mixing time, NOESY spectra with 200, 300 and 400 ms mixing times, ROESY spectra with 250 ms mixing time. 2D [^{1}H, ^{1}H] experiments were usually collected with number of scans ranging from 32 to 64, 256 FIDs in t1, 2048 data points in t2 and the suppression of the water signal was achieved by Excitation Sculpting [59]. NMR spectra were recorded just once for single peptide samples at the indicated concentrations.

Chemical shifts were referenced to the water signal at 4.7 ppm. The spectra were processed and analyzed with the software TopSpin 4.2 (Bruker, Milan, Italy) and NEASY [60] included in CARA (Computer Aided Resonance Assignment) (http://cara.nmr.ch/doku.php/). Proton resonance assignments were obtained following a standard protocol [36] by comparing TOCSY, NOESY and ROESY spectra except for the TTR^{45-52} peptide for which chemical shifts were assigned from the 2D [^{1}H, ^{1}H] TOCSY spectrum by comparison with assignments of the intact TTR^{34-52} peptide. Chemical shift deviations from random coil (rc) values for Hα protons (CSD = $\Delta\delta(H\alpha) = [\delta(H\alpha)\text{observed} - \delta(H\alpha)\text{rc}]$ were calculated following the approach of Kjaergaard and collaborators and random coil chemical shifts were retrieved using the primary peptide sequences as input, T=25 °C and pH values measured in each peptide sample, from the following website https://www1.bio.ku.dk/english/research/bms/sbinlab/randomchemicalshifts1 [38,39]. Percentages of helical population for each peptide were estimated with the following equation: $\%\ \text{Helix} = \{[(\delta H\alpha_{average}) / (-0.39)] \times 100\}$ [40] where $\delta H\alpha_{average} = [\delta(H\alpha)\text{obs} - \delta(H\alpha)\text{rc}]$ were averaged over residues with negative CSD values.

View Article Online
DOI: 10.1039/D5NR02939B

View Article Online
DOI: 10.1039/D5NR02939B

Author contributions

Mariantonietta Pizzella: Methodology, Investigation, Formal analysis; Antonella Accardo Conceptualization, Investigation, Writing – review & editing; Flavia Anna Mercurio: Methodology, Investigation, Formal analysis; Teresa Sibillano: Methodology, Investigation, Formal analysis; Enrico Gallo: Formal analysis, Writing – review & editing; Giancarlo Morelli: Formal analysis, Writing – review & editing; Giovanni Smaldone: Formal analysis, Writing – review & editing, Cinzia Giannini: Methodology, Formal analysis, Writing – review & editing; Marilisa Leone: Methodology, Formal analysis, Writing – review & editing, Nicole Balasco: Conceptualization, Formal analysis, Funding acquisition, Investigation, Validation, Writing – original draft, Carlo Diaferia: Conceptualization, Formal analysis, Funding acquisition, Investigation, Validation, Writing – original draft, Luigi Vitagliano: Conceptualization, Validation, Writing – original draft.

Conflicts of interest

The authors declare no conflict of interest.

Data availability

The coordinates of the experimental three-dimensional structures used in this project are freely accessible from the Protein Data Bank (PDB) at https://www.rcsb.org/. Authors will release MD trajectories upon article publication using the Zenodo repository (https://zenodo.org/).

Acknowledgments

We would like to thank Maurizio Amendola, Luca De Luca, Rocco Lassandro, Massimiliano Mazzocchi, and Giorgio Varriale for their technical support. The authors acknowledge Ministero dell'Università e della Ricerca, project PRIN_2022TSLMHR, titled "Biomaterials from peptide self-assembling generated by mimicking protein amyloid-like structures" funded by the European Union - Next Generation EU, Missione 4 Componente 1, CUP E53D23009550006, B53D23015710006. The CINECA award under the ISCRA initiative (ISCRA C project PDB-Pep ID HP10C2LWOA) is also acknowledged for the availability of high-performance computing resources and support.

View Article Online
DOI: 10.1039/D5NR02939B

Figure captions

Figure 1. Number of amyloid structures deposited in the Protein Data Bank (August 2024 release) from 2004 to 2024 (A). Bars are colored according to the techniques used to determine the structures: blue for X-ray diffraction, magenta for solid-state NMR, orange for electron microscopy, and green for electron crystallography. Number of amyloid structures as a function of size (number of amino acid residues) deposited during the periods 2004–2015, 2016–2020, and 2021–2024 (B).

Figure 2. Cartoon representation of the globular (A) and amyloid-like (B) structures of transthyretin (TTR, UniProtKB P02766). In the crystal structure of the TTR homotetramer (PDB ID: 6SUG) the N- and C-terminal ends of the four chains are highlighted in different colors. In the cryo-EM structure of a TTR amyloid fibril from the vitreous body of the eye (PDB ID: 7OB4) a dashed line represents the connection between two ends separated by residues that are not resolved in the structure. In both structures, the fragment 34–52 is highlighted in green.

Figure 3. Model of a single assembly of the TTR amyloid fibril. The model was generated based on PDB entry 7OB4, with additional layers added to extend it to ten (A). MD analyses conducted on the replica 1 simulation: RMSD values (calculated on the C^{α} atoms) for trajectory structures relative to the starting model (B); RMSF values (calculated on the C^{α} atoms) in the equilibrated region of the MD trajectory (50–200 ns). The average RMSF values of the C^{α} atoms for the four central layers of the entire assembly are displayed, with only residues exhibiting RMSF values below 0.6 Å included, RMSF values of residues of the fragment 34–52 are in green (C); time evolution of the secondary structure in the TTR assembly (D).

Figure 4. Model of the selected TTR fragments: the β-hairpin corresponding to residues 34-52, TTR^{34-52} (A), and the system composed by two individual strands, residues 34-40 and 45-52, TTR^{34-40}+TTR^{45-52} (B). The models were generated based on PDB entry 7OB4, with additional layers added to extend them to ten. Time evolution of the secondary structure in the simulations of TTR^{34-52} (C) and TTR^{34-40}+TTR^{45-52} (D).

Figure 5. Chemical formulas of peptides and fluorescence intensity of the ANS probe at 470 nm *versus* the concentration of: TTR^{34-40} (A), TTR^{45-52} (B), and TTR^{34-52} (C). CACs are deduced from the curve break points.

Figure 6. Hydrogel characterization. Inverted test tube (A) and rheological analysis of hydrogels: TTR^{34-40} (B), TTR^{45-52} (C), TTR^{34-52} (D), and TTR^{34-40}+TTR^{45-52} (E). Dynamic strain sweeps oscillatory test performed on hydrogels at 1%wt at 1 Hz frequency.

View Article Online
DOI: 10.1039/D5NR02939B

Figure 7: CD spectra of peptide hydrogels of TTR^{34-40} (A), TTR^{45-52} (B), TTR^{34-52} (C), and TTR^{34-40}+TTR^{45-52} (D) as a function of the temperature in the range from 30 to 80°C. Samples were prepared by the solvent-switch method at a concentration of 1%wt (10 mg/mL).

Figure 8: CD spectra of TTR^{34-40}(A), TTR^{45-52} (B), TTR^{34-52} (C), and TTR^{34-40}+TTR^{45-52} (D) as a function of the temperature in the range from 30 to 80°C. Samples were prepared by the solvent-switch method at a concentration of 0.1%wt (1 mg/mL).

Figure 9. UV-Vis spectra of Congo Red alone and co-incubated with peptide solutions at a concentration of 5.0 mg/mL (A). Subtracted UV-Vis spectra, obtained by subtracting the spectrum of Congo Red alone from those of the peptide solutions (B).

Figure 10. Structural models of TTR^{34-52}, TTR^{34-40}, TTR^{45-52}, and TTR^{34-40}+TTR^{45-52}, presented as single-chain or multi-chain assemblies, predicted using the AlphaFold3 algorithm (https://alphafoldserver.com/). The models are colored according to the AlphaFold per-residue confidence metric (pLDDT) as follows: blue for pLDDT > 90, cyan for 70 < pLDDT ≤ 90, yellow for 50 < pLDDT ≤ 70, and orange for pLDDT < 50. For the TTR^{34-40}+TTR^{45-52} multi-chain system, a representation highlighting the two distinct peptides with different colors (magenta for TTR^{34-40} and green for TTR^{45-52}) is shown.

Figure 11. Time evolution of the secondary structure of TTR^{34-52} (A), TTR^{34-40} (B), TTR^{45-52} (C), and TTR^{34-40}+TTR^{45-52} (D) as single-chain models and TTR^{34-40} (E), TTR^{45-52} (F), and TTR^{34-40}+TTR^{45-52} (G) as multi-chain assemblies in the simulations (replica 1) conducted starting from the AF predicted models.

Figure 12. Selected SEM microphotos of peptide xerogels of TTR^{34-40} (A, B), TTR^{45-52} (C, D), TTR^{34-52} (E, F), and TTR^{34-40}+TTR^{45-52} (G, H) prepared from hydrogels at 1.0 %wt. Scale bar and magnification are 50 μm, 3000x for A, C, E, G and 15 μm, 9600x for B, D, F, H, respectively.

Figure 13. 2D WAXS patterns of TTR^{34-52}(A), TTR^{34-40}(B), TTR^{45-52}(C) and TTR^{35-40}+TTR^{45-52}(D) and the corresponding 1D profiles along the meridional (E) and equatorial (F) directions.

Figure 14. Fluorescence Microscopy of TTR^{34-40} (A), TTR^{45-52} (B), TTR^{34-52} (C) and TTR^{34-40}+TTR^{45-52} (D): bright field images and fluorescence images excited in the spectral regions of GFP (λ_{exc}=488 nm, λ_{em} =507 nm), DAPI (λ_{exc}=359 nm, λ_{em}=461nm), and rhodamine (λ_{exc}=359 nm, λ_{em}=461nm) filters.

View Article Online
DOI: 10.1039/D5NR02939B

Tables

Table 1: CAC values, expressed in mol/L and mg/mL for TTR^{34-52} and the two shorter fragments TTR^{34-40} and TTR^{45-52}. CAC values have been determined at the break point of the plots reporting the fluorescence intensity of ANS fluorophore at 470 nm as a function of the peptide concentration.

Peptide	CAC (mol/L)	CAC (mg/mL)	LogP
TTR^{34-40}	$5.48 \cdot 10^{-4}$	0.429	0.45 ± 0.87
TTR^{45-52}	$2.36 \cdot 10^{-4}$	0.211	-1.21 ± 0.95
TTR^{34-52}	$1.11 \cdot 10^{-4}$	0.223	-1.27 ± 1.10

Table 2. WAXS Reflections and d-spacing.

Reflection	Samples	q ($Å^{-1}$)	d (Å)
Meridional	TTR^{34-52}, TTR^{34-40}, TTR^{45-52}, TTR^{34-40}+TTR^{45-52}	1.32 ± 0.02	4.7 ± 0.5
	TTR^{34-52}, TTR^{45-52}, TTR^{34-40}+TTR^{45-52}	1.68 ± 0.02	3.7 ± 0.5
Equatorial	TTR^{34-52}, TTR^{45-52}, TTR^{34-40}+TTR^{45-52}	0.55–0.65 ± 0.02	9.6–11.4 ± 0.5
	TTR^{34-40}	0.42 ± 0.02	14.9 ± 0.5
	TTR^{34-40}	0.70 ± 0.02	8.9 ± 0.5
	TTR^{34-40}	1.20 ± 0.02	5.2 ± 0.5
	TTR^{34-40}	1.97 ± 0.02	3.2 ± 0.5

References

1 P. C. Ke, R. Zhou, L. C. Serpell, R. Riek, T. P. J. Knowles, H. A. Lashuel, E. Gazit, I. W. Hamley, T. P. Davis, M. Fändrich, D. E. Otzen, M. R. Chapman, C. M. Dobson, D. S. Eisenberg and R. Mezzenga, *Chem. Soc. Rev.*, 2020, **49**, 5473–5509.

2 N. Balasco, C. Diaferia, G. Morelli, L. Vitagliano and A. Accardo, *Front. Bioeng. Biotechnol.*, 2021, **9**, 641372.

3 F. Chiti and C. M. Dobson, *Annu. Rev. Biochem.*, 2017, **86**, 27–68.

4 M. Reches and E. Gazit, *Science*, 2003, **300**, 625–627.

5 I. W. Hamley, *Chem. Rev.*, 2017, **117**, 14015–14041.

6 I. Cherny and E. Gazit, *Angew Chem Int Ed*, 2008, **47**, 4062–4069.

7 F. T. S. Chan, G. S. Kaminski Schierle, J. R. Kumita, C. W. Bertoncini, C. M. Dobson and C. F. Kaminski, *Analyst*, 2013, **138**, 2156.

8 C. W. Chung, A. D. Stephens, E. Ward, Y. Feng, M. J. Davis, C. F. Kaminski and G. S. Kaminski Schierle, *Anal. Chem.*, 2022, **94**, 5367–5374.

9 G. D. Mirón, J. A. Semelak, L. Grisanti, A. Rodriguez, I. Conti, M. Stella, J. Velusamy, N. Seriani, N. Došlić, I. Rivalta, M. Garavelli, D. A. Estrin, G. S. Kaminski Schierle, M. C. González Lebrero, A. Hassanali and U. N. Morzan, *Nat Commun*, 2023, **14**, 7325.

10 N. Balasco, C. Diaferia, E. Rosa, A. Monti, M. Ruvo, N. Doti and L. Vitagliano, *IJMS*, 2023, **24**, 8372.

11 C. Diaferia, T. Sibillano, N. Balasco, C. Giannini, V. Roviello, L. Vitagliano, G. Morelli and A. Accardo, *Chemistry A European J*, 2016, **22**, 16586–16597.

12 C. Diaferia, N. Balasco, T. Sibillano, M. Ghosh, L. Adler-Abramovich, C. Giannini, L. Vitagliano, G. Morelli and A. Accardo, *Chemistry A European J*, 2018, **24**, 6804–6817.

13 C. Diaferia, T. Sibillano, C. Giannini, V. Roviello, L. Vitagliano, G. Morelli and A. Accardo, *Chemistry A European J*, 2017, **23**, 8741–8748.

14 C. Diaferia, T. Sibillano, D. Altamura, V. Roviello, L. Vitagliano, C. Giannini, G. Morelli and A. Accardo, *Chemistry A European J*, 2017, **23**, 14039–14048.

15 C. Schiattarella, C. Diaferia, E. Gallo, B. Della Ventura, G. Morelli, L. Vitagliano, R. Velotta and A. Accardo, *Sci Rep*, 2022, **12**, 759.

16 U. N. Morzan, G. Díaz Mirón, L. Grisanti, M. C. González Lebrero, G. S. Kaminski Schierle and A. Hassanali, *J. Phys. Chem. B*, 2022, **126**, 7203–7211.

17 E. Mayans and C. Alemán, *Molecules*, 2020, **25**, 6037.

18 M. C. Cringoli and S. Marchesan, *Molecules*, 2023, **28**, 4970.

19 K. Tao, A. Levin, L. Adler-Abramovich and E. Gazit, *Chem. Soc. Rev.*, 2016, **45**, 3935–3953.

20 S. K. Burley, H. M. Berman, G. J. Kleywegt, J. L. Markley, H. Nakamura and S. Velankar, in *Protein Crystallography*, eds. A. Wlodawer, Z. Dauter and M. Jaskolski, Springer New York, New York, NY, 2017, vol. 1607, pp. 627–641.

21 X. Bai, G. McMullan and S. H. W. Scheres, *Trends in Biochemical Sciences*, 2015, **40**, 49–57.

22 E. Callaway, *Nature*, 2015, **525**, 172–174.

23 L. Poli, B. Labella, S. Cotti Piccinelli, F. Caria, B. Risi, S. Damioli, A. Padovani and M. Filosto, *Front. Neurol.*, 2023, **14**, 1242815.

24 M. A. Liz, T. Coelho, V. Bellotti, M. I. Fernandez-Arias, P. Mallaina and L. Obici, *Neurol Ther*, 2020, **9**, 395–402.

25 S. Raimondi, P. P. Mangione, G. Verona, D. Canetti, P. Nocerino, L. Marchese, R. Piccarducci, V. Mondani, G. Faravelli, G. W. Taylor, J. D. Gillmore, A. Corazza, M. B. Pepys, S. Giorgetti and V. Bellotti, *Journal of Biological Chemistry*, 2020, **295**, 11379–11387.
26 V. Loconte, M. Cianci, I. Menozzi, D. Sbravati, F. Sansone, A. Casnati and R. Berni, *Bioorganic Chemistry*, 2020, **103**, 104144.
27 I. Iakovleva, M. Hall, M. Oelker, L. Sandblad, I. Anan and A. E. Sauer-Eriksson, *Nat Commun*, 2021, **12**, 7141.
28 C. Diaferia, E. Gianolio, A. Accardo and G. Morelli, *Journal of Peptide Science*, 2017, **23**, 122–130.
29 E. Fuentes, K. Boháčová, A. M. Fuentes-Caparrós, R. Schweins, E. R. Draper, D. J. Adams, S. Pujals and L. Albertazzi, *Chemistry A European J*, 2020, **26**, 9869–9873.
30 A. Rodger, R. Marrington, D. Roper and S. Windsor, in *Protein-Ligand Interactions*, ed. G. Ulrich Nienhaus, Humana Press, Totowa, NJ, 2005, vol. 305, pp. 343–363.
31 M. E. Holtzer and A. Holtzer, *Biopolymers*, 1992, **32**, 1675–1677.
32 W. E. Klunk, R. F. Jacob and R. P. Mason, *Analytical Biochemistry*, 1999, **266**, 66–76.
33 A. Kumar, R. R. Ernst and K. Wüthrich, *Biochemical and Biophysical Research Communications*, 1980, **95**, 1–6.
34 D. Marion, *FEBS Letters*, 1985, **192**, 99–103.
35 C. Griesinger, G. Otting, K. Wuethrich and R. R. Ernst, *J. Am. Chem. Soc.*, 1988, **110**, 7870–7872.
36 K. Wüthrich, *NMR of proteins and nucleic acids*, Wiley, New York, 1986.
37 D. S. Wishart, B. D. Sykes and F. M. Richards, *FEBS Letters*, 1991, **293**, 72–80.
38 M. Kjaergaard, S. Brander and F. M. Poulsen, *J Biomol NMR*, 2011, **49**, 139–149.
39 M. Kjaergaard and F. M. Poulsen, *J Biomol NMR*, 2011, **50**, 157–165.
40 J. Pimenta, A. Viegas, J. Sardinha, I. C. Martins, E. J. Cabrita, C. M. G. A. Fontes, J. A. Prates and R. M. L. N. Pereira, *Peptides*, 2013, **49**, 32–40.
41 C. Diaferia, C. Avitabile, M. Leone, E. Gallo, M. Saviano, A. Accardo and A. Romanelli, *Chemistry A European J*, 2021, **27**, 14307–14316.
42 A. Mosseri, M. Sancho-Albero, M. Leone, D. Nava, F. Secundo, D. Maggioni, L. De Cola and A. Romanelli, *Chemistry A European J*, 2022, **28**, e202200693.
43 J. Abramson, J. Adler, J. Dunger, R. Evans, T. Green, A. Pritzel, O. Ronneberger, L. Willmore, A. J. Ballard, J. Bambrick, S. W. Bodenstein, D. A. Evans, C.-C. Hung, M. O'Neill, D. Reiman, K. Tunyasuvunakool, Z. Wu, A. Žemgulytė, E. Arvaniti, C. Beattie, O. Bertolli, A. Bridgland, A. Cherepanov, M. Congreve, A. I. Cowen-Rivers, A. Cowie, M. Figurnov, F. B. Fuchs, H. Gladman, R. Jain, Y. A. Khan, C. M. R. Low, K. Perlin, A. Potapenko, P. Savy, S. Singh, A. Stecula, A. Thillaisundaram, C. Tong, S. Yakneen, E. D. Zhong, M. Zielinski, A. Žídek, V. Bapst, P. Kohli, M. Jaderberg, D. Hassabis and J. M. Jumper, *Nature*, 2024, **630**, 493–500.
44 V. Mariani, M. Biasini, A. Barbato and T. Schwede, *Bioinformatics*, 2013, **29**, 2722–2728.
45 H. Ramli, N. F. A. Zainal, M. Hess and C. H. Chan, *Chemistry Teacher International*, 2022, **4**, 307–326.
46 L. P. DeFlores, Z. Ganim, R. A. Nicodemus and A. Tokmakoff, *J. Am. Chem. Soc.*, 2009, **131**, 3385–3391.
47 C. Diaferia, C. Schiattarella, E. Gallo, B. Della Ventura, G. Morelli, R. Velotta, L. Vitagliano and A. Accardo, *ChemPhysChem*, 2021, **22**, 2215–2221.

View Article Online
DOI: 10.1039/D5NR02939B

48 S. R. S. Veloso, M. Rosa, C. Diaferia and C. Fernandes, *Gels*, 2024, **10**, 507.
49 P. Makam and E. Gazit, *Chem. Soc. Rev.*, 2018, **47**, 3406–3420.
50 D. Van Der Spoel, E. Lindahl, B. Hess, G. Groenhof, A. E. Mark and H. J. C. Berendsen, *J Comput Chem*, 2005, **26**, 1701–1718.
51 T. Darden, D. York and L. Pedersen, *The Journal of Chemical Physics*, 1993, **98**, 10089–10092.
52 W. Humphrey, A. Dalke and K. Schulten, *Journal of Molecular Graphics*, 1996, **14**, 33–38.
53 G. Nagy, M. Igaev, N. C. Jones, S. V. Hoffmann and H. Grubmüller, *J. Chem. Theory Comput.*, 2019, **15**, 5087–5102.
54 M. Sunde, L. C. Serpell, M. Bartlam, P. E. Fraser, M. B. Pepys and C. C. F. Blake, *Journal of Molecular Biology*, 1997, **273**, 729–739.
55 R. Wakabayashi, R. Imatani, M. Katsuya, Y. Higuchi, H. Noguchi, N. Kamiya and M. Goto, *Chem. Commun.*, 2022, **58**, 585–588.
56 D. Altamura, R. Lassandro, F. A. Vittoria, L. De Caro, D. Siliqi, M. Ladisa and C. Giannini, *J Appl Crystallogr*, 2012, **45**, 869–873.
57 T. Sibillano, L. De Caro, D. Altamura, D. Siliqi, M. Ramella, F. Boccafoschi, G. Ciasca, G. Campi, L. Tirinato, E. Di Fabrizio and C. Giannini, *Sci Rep*, 2014, **4**, 6985.
58 U. Piantini, O. W. Sorensen and R. R. Ernst, *J. Am. Chem. Soc.*, 1982, **104**, 6800–6801.
59 T. L. Hwang and A. J. Shaka, *Journal of Magnetic Resonance, Series A*, 1995, **112**, 275–279.
60 C. Bartels, T. Xia, M. Billeter, P. Güntert and K. Wüthrich, *J Biomol NMR*, 1995, **6**, 1–10.

View Article Online
DOI: 10.1039/D5NR02939B

Data availability

The coordinates of the experimental three-dimensional structures used in this project are freely accessible from the Protein Data Bank (PDB) at https://www.rcsb.org/. Authors will release MD trajectories upon article publication using the Zenodo repository (https://zenodo.org/).

View Article Online
DOI: 10.1039/D5NR02939B

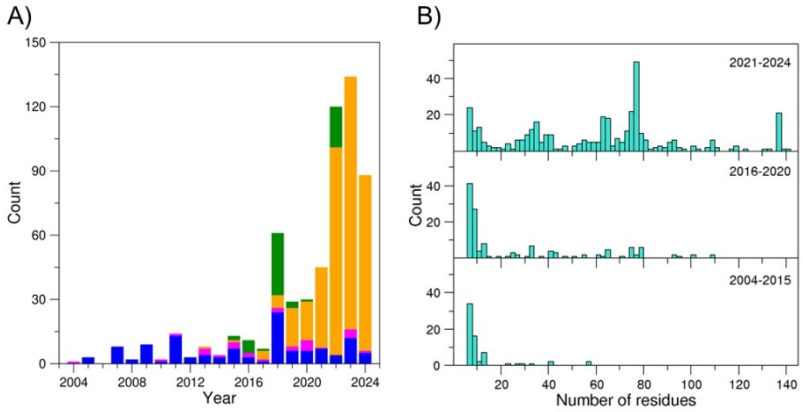

Figure 1. Number of amyloid structures deposited in the Protein Data Bank (August 2024 release) from 2004 to 2024 (A). Bars are colored according to the techniques used to determine the structures: blue for X-ray diffraction, magenta for solid-state NMR, orange for electron microscopy, and green for electron crystallography. Number of amyloid structures as a function of size (number of amino acid residues) deposited during the periods 2004–2015, 2016–2020, and 2021–2024 (B).

108x60mm (300 x 300 DPI)

View Article Online
DOI: 10.1039/D5NR02939B

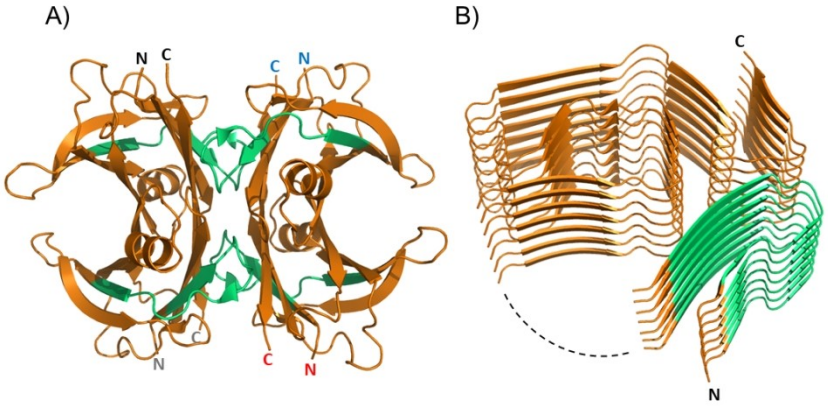

Figure 2. Cartoon representation of the globular (A) and amyloid-like (B) structures of transthyretin (TTR, UniProtKB P02766). In the crystal structure of the TTR homotetramer (PDB ID: 6SUG) the N- and C-terminal ends of the four chains are highlighted in different colors. In the cryo-EM structure of a TTR amyloid fibril from the vitreous body of the eye (PDB ID: 7OB4) a dashed line represents the connection between two ends separated by residues that are not resolved in the structure. In both structures, the fragment 34–52 is highlighted in green.

108x60mm (300 x 300 DPI)

View Article Online
DOI: 10.1039/D5NR02939B

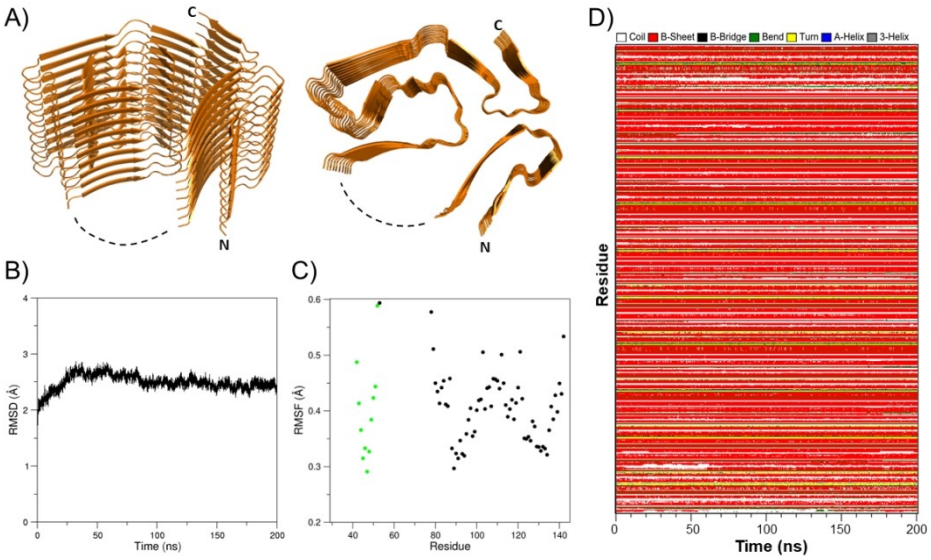

Model of a single assembly of the TTR amyloid fibril. The model was generated based on PDB entry 7OB4, with additional layers added to extend it to ten (A). MD analyses conducted on the replica 1 simulation: RMSD values (calculated on the Cα atoms) for trajectory structures relative to the starting model (B); RMSF values (calculated on the Cα atoms) in the equilibrated region of the MD trajectory (50–200 ns). The average RMSF values of the Cα atoms for the four central layers of the entire assembly are displayed, with only residues exhibiting RMSF values below 0.6 Å included, RMSF values of residues of the fragment 34–52 are in green (C); time evolution of the secondary structure in the TTR assembly (D).

108x60mm (300 x 300 DPI)

View Article Online
DOI: 10.1039/D5NR02939B

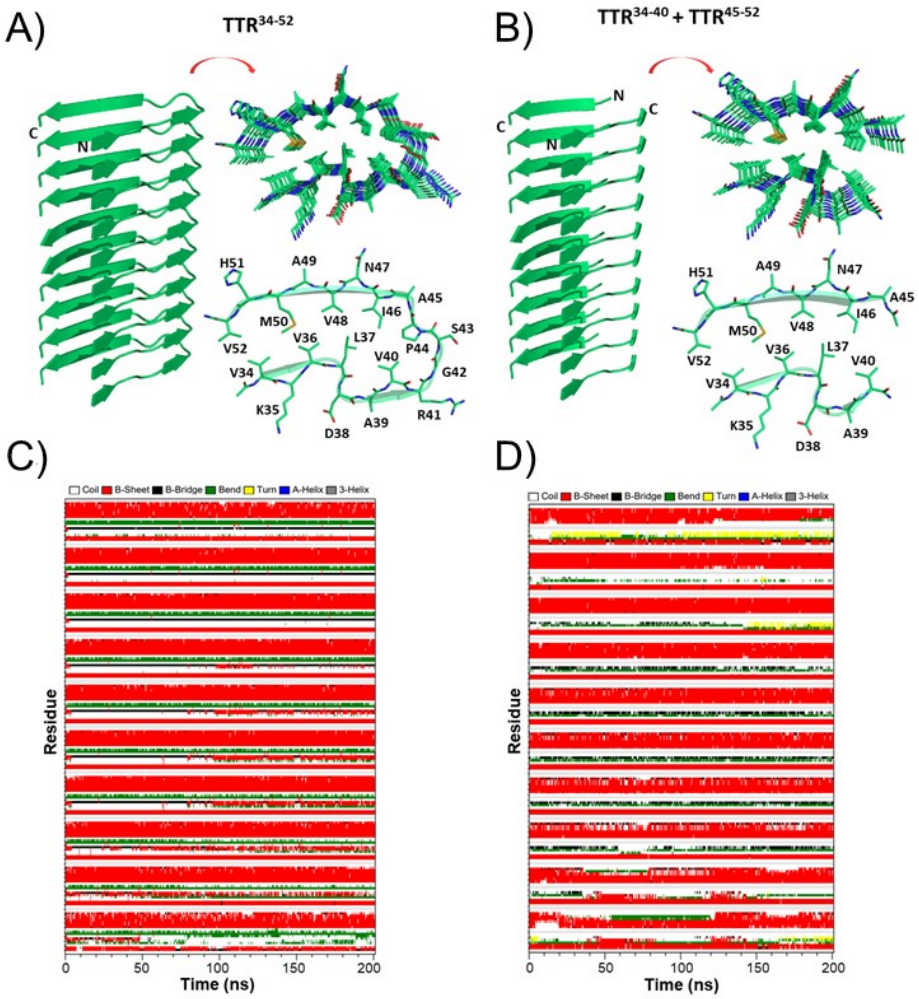

Figure 4. Model of the selected TTR fragments: the β-hairpin corresponding to residues 34-52, TTR34-52 (A), and the system composed by two individual strands, residues 34-40 and 45-52, TTR34-40+TTR45-52 (B). The models were generated based on PDB entry 7OB4, with additional layers added to extend them to ten. Time evolution of the secondary structure in the simulations of TTR34-52 (C) and TTR34-40+TTR45-52 (D).

66x67mm (300 x 300 DPI)

View Article Online
DOI: 10.1039/D5NR02939B

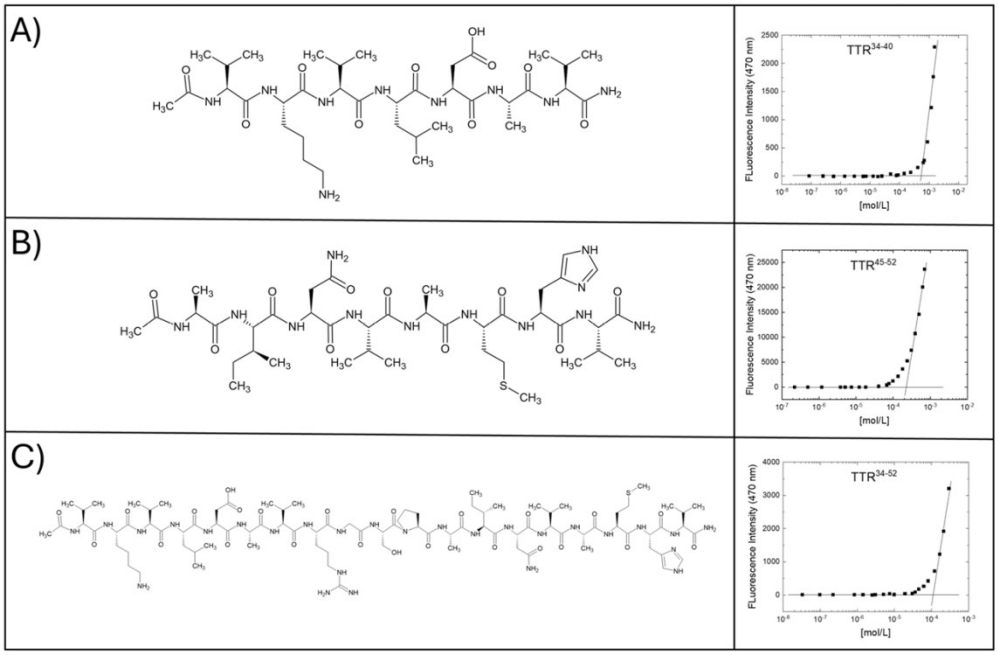

Figure 5. Chemical formulas of peptides and fluorescence intensity of the ANS probe at 470 nm versus the concentration of: TTR34-40 (A), TTR45-52 (B), and TTR34-52 (C). CACs are deduced from the curve break points.

111x72mm (300 x 300 DPI)

View Article Online
DOI: 10.1039/D5NR02939B

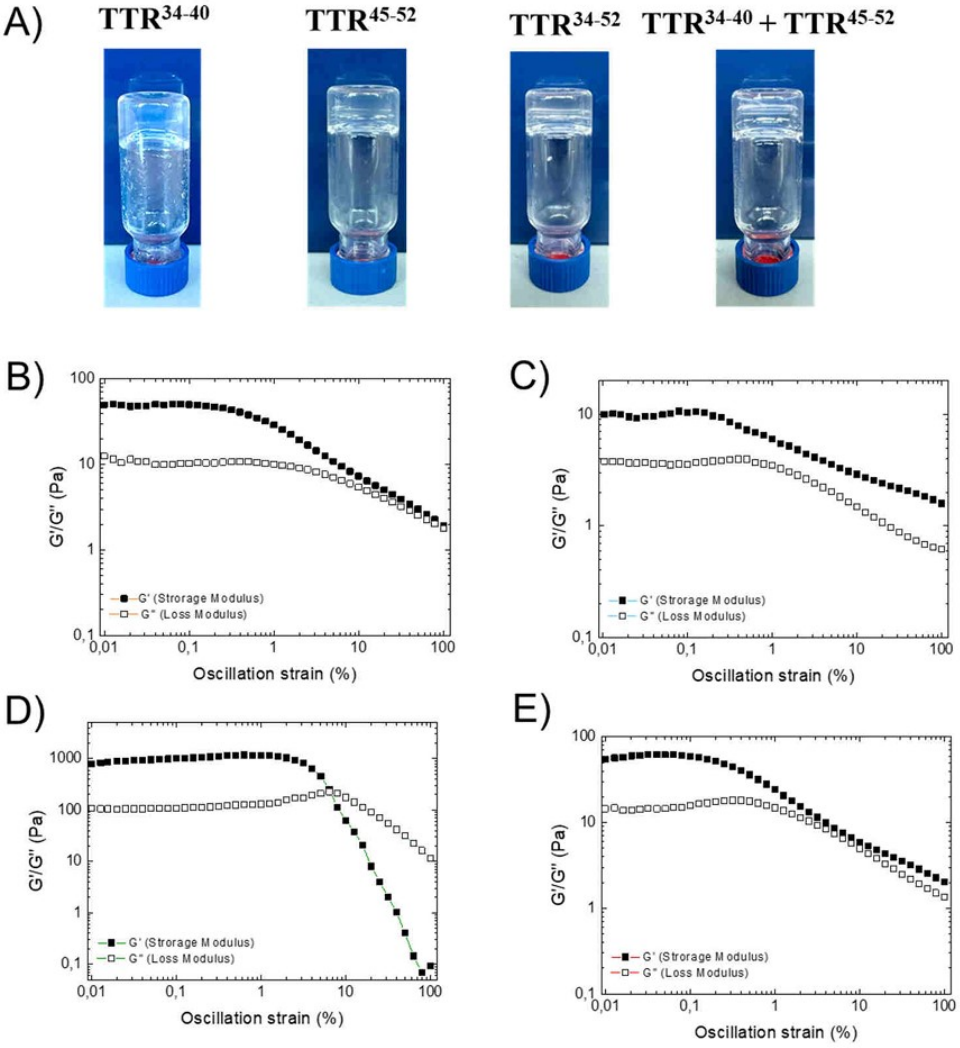

Figure 6. Hydrogel characterization. Inverted test tube (A) and rheological analysis of hydrogels: TTR34-40 (B), TTR45-52 (C), TTR34-52 (D), and TTR34-40+TTR45-52 (E). Dynamic strain sweeps oscillatory test performed on hydrogels at 1%wt at 1 Hz frequency.

75x80mm (300 x 300 DPI)

View Article Online
DOI: 10.1039/D5NR02939B

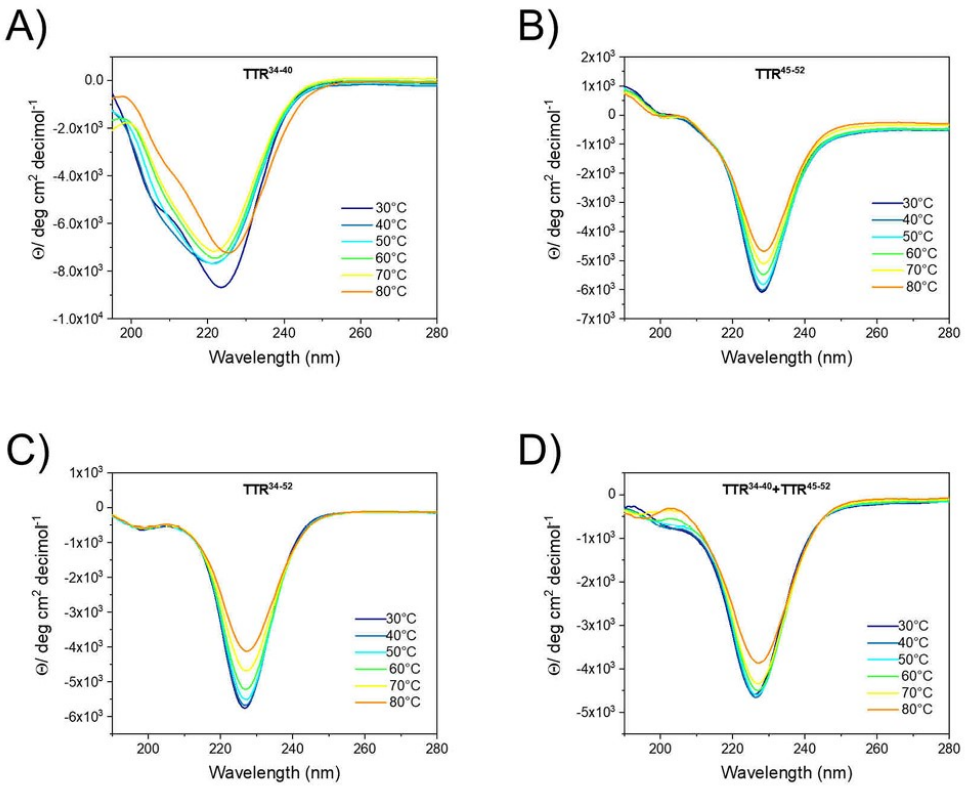

Figure 7: CD spectra of peptide hydrogels of TTR34-40 (A), TTR45-52 (B), TTR34-52 (C), and TTR34-40+TTR45-52 (D) as a function of the temperature in the range from 30 to 80°C. Samples were prepared by the solvent-switch method at a concentration of 1%wt (10 mg/mL).

82x67mm (300 x 300 DPI)

View Article Online
DOI: 10.1039/D5NR02939B

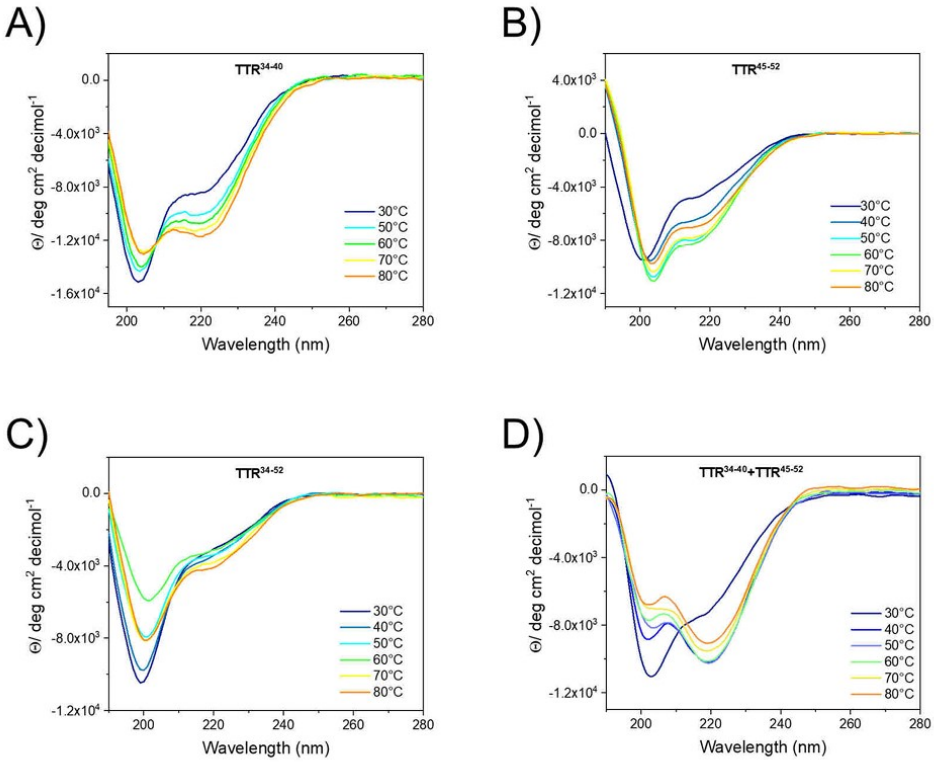

Figure 8: CD spectra of TTR34-40(A), TTR45-52 (B), TTR34-52 (C), and TTR34-40+TTR45-52 (D) as a function of the temperature in the range from 30 to 80°C. Samples were prepared by the solvent-switch method at a concentration of 0.1%wt (1 mg/mL).

83x68mm (300 x 300 DPI)

View Article Online
DOI: 10.1039/D5NR02939B

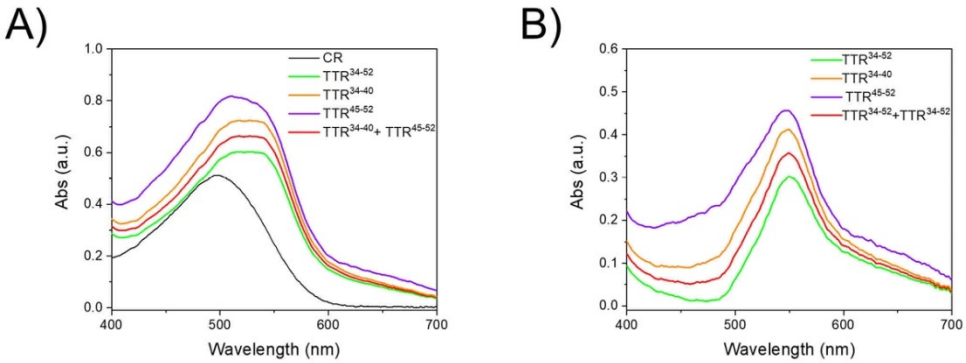

Figure 9. UV-Vis spectra of Congo Red alone and co-incubated with peptide solutions at a concentration of 5.0 mg/mL (A). Subtracted UV-Vis spectra, obtained by subtracting the spectrum of Congo Red alone from those of the peptide solutions (B).

104x39mm (300 x 300 DPI)

View Article Online
DOI: 10.1039/D5NR02939B

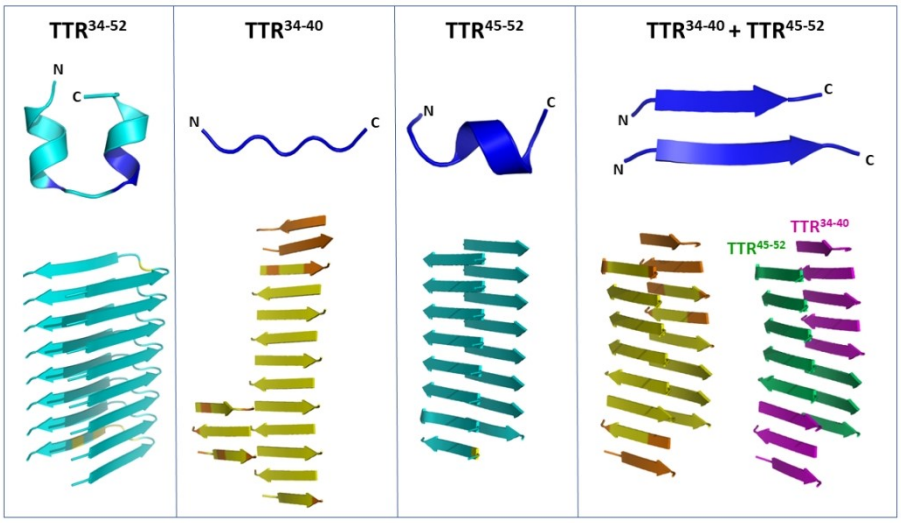

Figure 10. Structural models of TTR34-52, TTR34-40, TTR45-52, and TTR34-40+TTR45-52, presented as single-chain or multi-chain assemblies, predicted using the AlphaFold3 algorithm (https://alphafoldserver.com/). The models are colored according to the AlphaFold per-residue confidence metric (pLDDT) as follows: blue for pLDDT > 90, cyan for 70 < pLDDT ≤ 90, yellow for 50 < pLDDT ≤ 70, and orange for pLDDT < 50. For the TTR34-40+TTR45-52 multi-chain system, a representation highlighting the two distinct peptides with different colors (magenta for TTR34-40 and green for TTR45-52) is shown.

108x60mm (300 x 300 DPI)

View Article Online
DOI: 10.1039/D5NR02939B

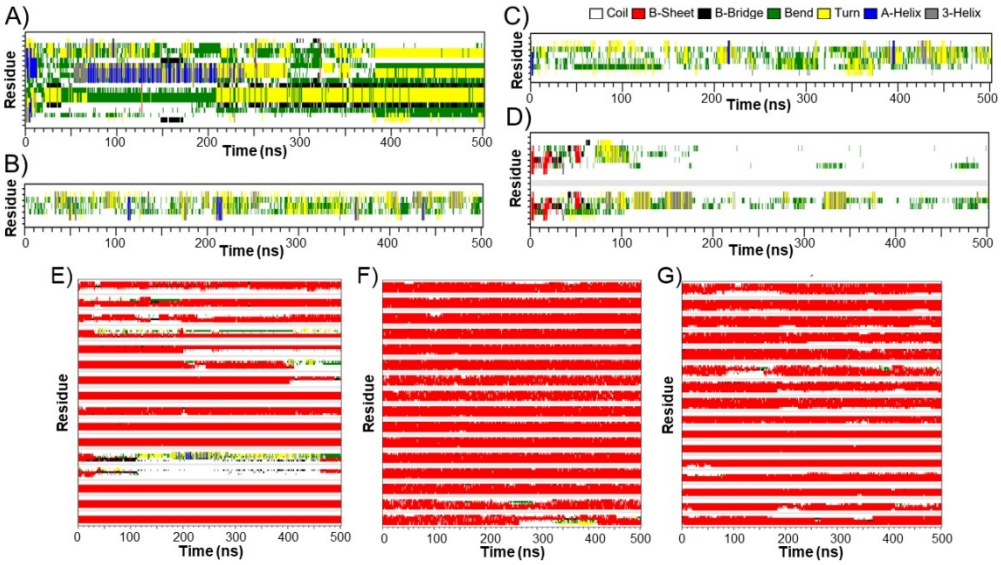

Time evolution of the secondary structure of TTR34-52 (A), TTR34-40 (B), TTR45-52 (C), and TTR34-40+TTR45-52 (D) as single-chain models and TTR34-40 (E), TTR45-52 (F), and TTR34-40+TTR45-52 (G) as multi-chain assemblies in the simulations (replica 1) conducted starting from the AF predicted models.

108x60mm (300 x 300 DPI)

View Article Online
DOI: 10.1039/D5NR02939B

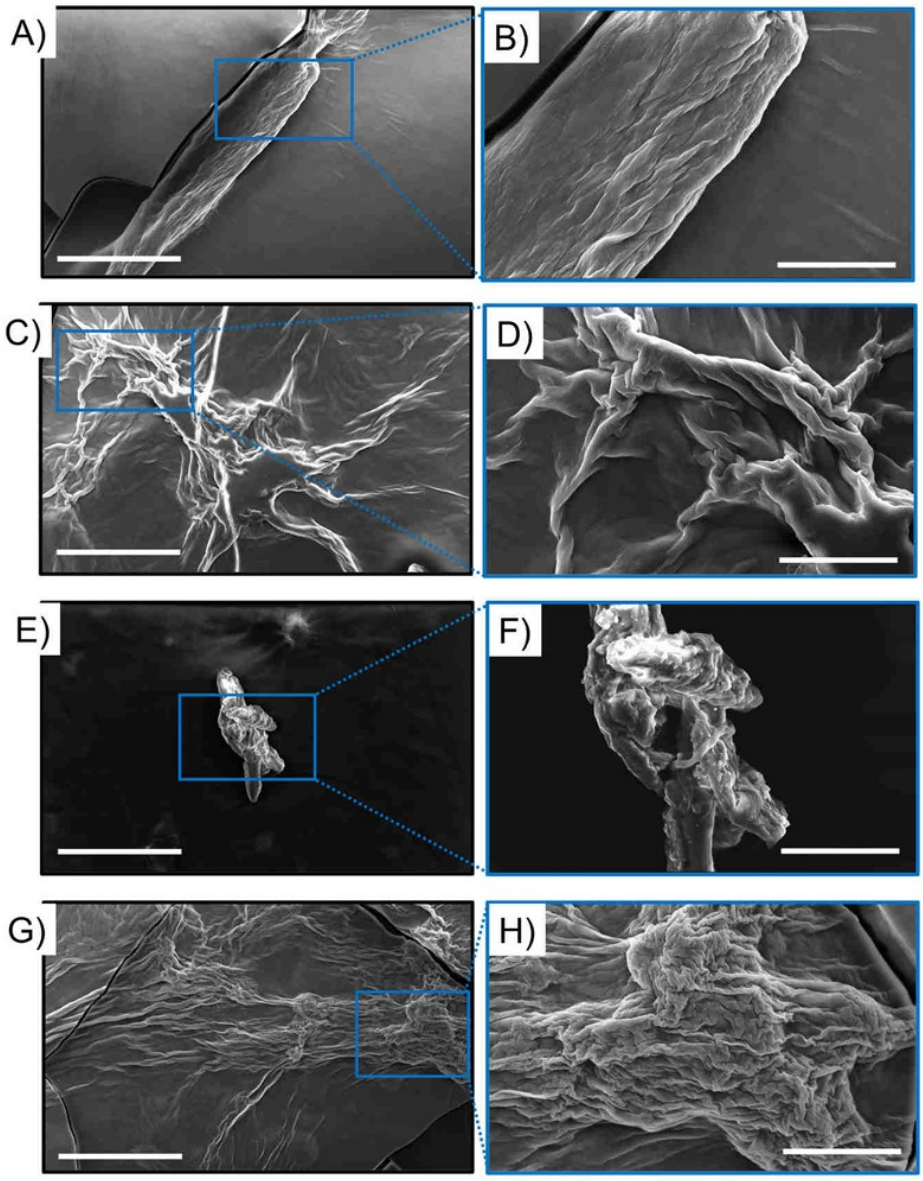

Figure 12. Selected SEM microphotos of peptide xerogels of TTR34-40 (A, B), TTR45-52 (C, D), TTR34-52 (E, F), and TTR34-40+TTR45-52 (G, H) prepared from hydrogels at 1.0 %wt. Scale bar and magnification are 50 μm, 3000x for A, C, E, G and 15 μm, 9600x for B, D, F, H, respectively.

67x85mm (300 x 300 DPI)

View Article Online
DOI: 10.1039/D5NR02939B

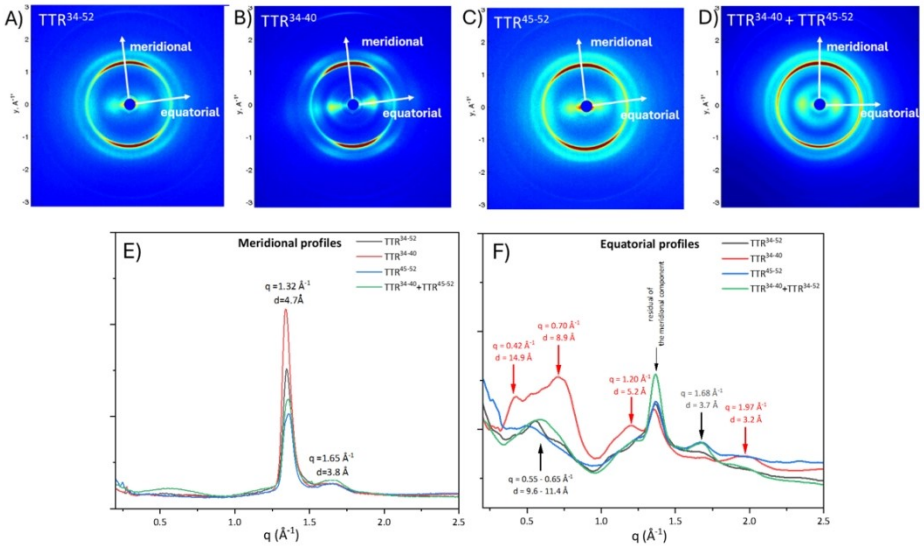

Figure 13. 2D WAXS patterns of TTR34-52(A), TTR34-40(B), TTR45-52(C) and TTR35-40+TTR45-52(D) and the corresponding 1D profiles along the meridional (E) and equatorial (F) directions.

108x60mm (300 x 300 DPI)

View Article Online
DOI: 10.1039/D5NR02939B

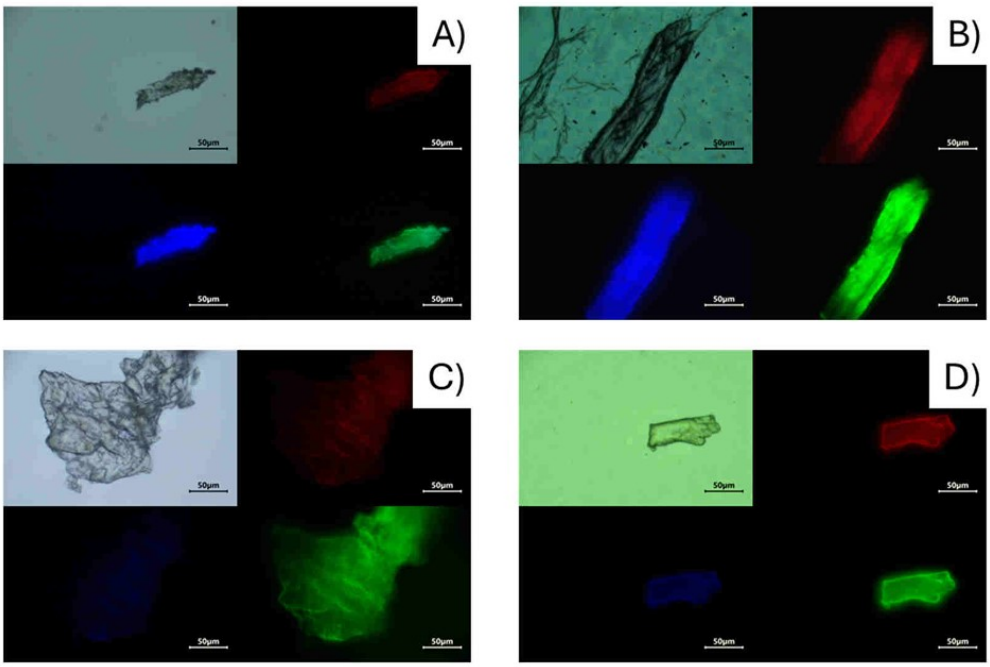

Figure 14. Fluorescence Microscopy of TTR34-40 (A), TTR45-52 (B), TTR34-52 (C) and TTR34-40 + TTR45-52 (D): bright field images and fluorescence images excited in the spectral regions of GFP (λexc=488 nm, λem =507 nm), DAPI (λexc=359 nm, λem=461nm), and rhodamine (λexc=359 nm, λem=461nm) filters.

79x53mm (300 x 300 DPI)